JOURNAL OF GEOPHYSICAL RESEARCH, VOL. 115, B02405, doi:10.1029/2009JB006429, 2010

Source model of the 2007 M_w 8.0 Pisco, Peru earthquake: Implications for seismogenic behavior of subduction megathrusts

A. Sladen,[1] H. Tavera,[2] M. Simons,[3] J. P. Avouac,[1] A. O. Konca,[3] H. Perfettini,[4] L. Audin,[5,6] E. J. Fielding,[7] F. Ortega,[3] and R. Cavagnoud[8]

Received 3 March 2009; revised 24 June 2009; accepted 4 September 2009; published 9 February 2010.

[1] We use Interferometric Synthetic Aperture Radar, teleseismic body waves, tsunami waveforms recorded by tsunameters, field observations of coastal uplift, subsidence, and runup to develop and test a refined model of the spatiotemporal history of slip during the M_w 8.0 Pisco earthquake of 15 August 2007. Our preferred solution shows two distinct patches of high slip. One patch is located near the epicenter while another larger patch ruptured 60 km further south, at the latitude of the Paracas peninsula. Slip on the second patch started 60 s after slip initiated on the first patch. We observed a remarkable anticorrelation between the coseismic slip distribution and the aftershock distribution determined from the Peruvian seismic network. The proposed source model is compatible with regional runup measurements and open ocean tsunami records. From the latter data set, we identified the 12 min timing error of the tsunami forecast system as being due to a mislocation of the source, caused by the use of only one tsunameter located in a nonoptimal azimuth. The comparison of our source model with the tsunami observations validate that the rupture did not extend to the trench and confirms that the Pisco event is not a tsunami earthquake despite its low apparent rupture velocity (<1.5 km/s). We favor the interpretation that the earthquake consists of two subevents, each with a conventional rupture velocity (2–4 km/s). The delay between the two subevents might reflect the time for the second shock to nucleate or, alternatively, the time it took for afterslip to increase the stress level on the second asperity to a level necessary for static triggering. The source model predicts uplift offshore and subsidence on land with the pivot line following closely the coastline. This pattern is consistent with our observation of very small vertical displacement along the shoreline when we visited the epicentral area in the days following the event. This earthquake represents, to our knowledge, one of the best examples of a link between the geomorphology of the coastline and the pattern of surface deformation induced by large interplate ruptures.

Citation: Sladen, A., H. Tavera, M. Simons, J. P. Avouac, A. O. Konca, H. Perfettini, L. Audin, E. J. Fielding, F. Ortega, and R. Cavagnoud (2010), Source model of the 2007 M_w 8.0 Pisco, Peru earthquake: Implications for seismogenic behavior of subduction megathrusts, *J. Geophys. Res.*, *115*, B02405, doi:10.1029/2009JB006429.

1. Introduction

[2] The western margin of South America regularly experiences large subduction zone earthquakes as a result of the approximately 7 cm/yr convergence between the Nazca and South American plates [e.g., *Sella et al.*, 2002]. We focus on one such event that occurred in central Peru, offshore of the city of Pisco (Figure 1) on 15 August 2007 and reached a magnitude of M_w 8.0 producing local destruction and a regional tsunami [*Pritchard and Fielding*, 2008; *Wei et al.*, 2008; *Fritz et al.*, 2008]. The seismotectonic setting in this area is particularly interesting. The earthquake occurred just north of where the Nazca ridge encounters the trench and is being subducted obliquely beneath the Peruvian forearc (Figure 1). This area coincides with the transition from a regular steeply dipping subduction zone to the southeast to a flat subduction zone to the northwest [*Cahill and Isacks*, 1992]. Also, there are well-developed offshore forearc basins north of the Nazca Ridge while there are none south of the ridge [*Clift et al.*, 2003; *Krabbenhoft et al.*, 2004]. Finally, the Pisco area also coincides with a very distinct kink of the coastline. As result, the distance between the trench and the coastline increases from ~100 km, south of Pisco, to

[1]Tectonics Observatory, Division of Geological and Planetary Sciences, California Institute of Technology, Pasadena, California, USA.
[2]Instituto Geofísico del Perú, Lima, Peru.
[3]Seismological Laboratory, California Institute of Technology, Pasadena, California, USA.
[4]Laboratoire de Géophysique Interne et de Tectonophysique, Université Joseph Fourier, IRD, Grenoble, France.
[5]LMTG, Université de Toulouse, UPS, Toulouse, France.
[6]LMTG, IRD, Toulouse, France.
[7]Jet Propulsion Laboratory, California Institute of Technology, Pasadena, California, USA.
[8]Instituto Francés de Estudios Andinos, Lima, Peru.

0148-0227/10/2009JB006429$09.00

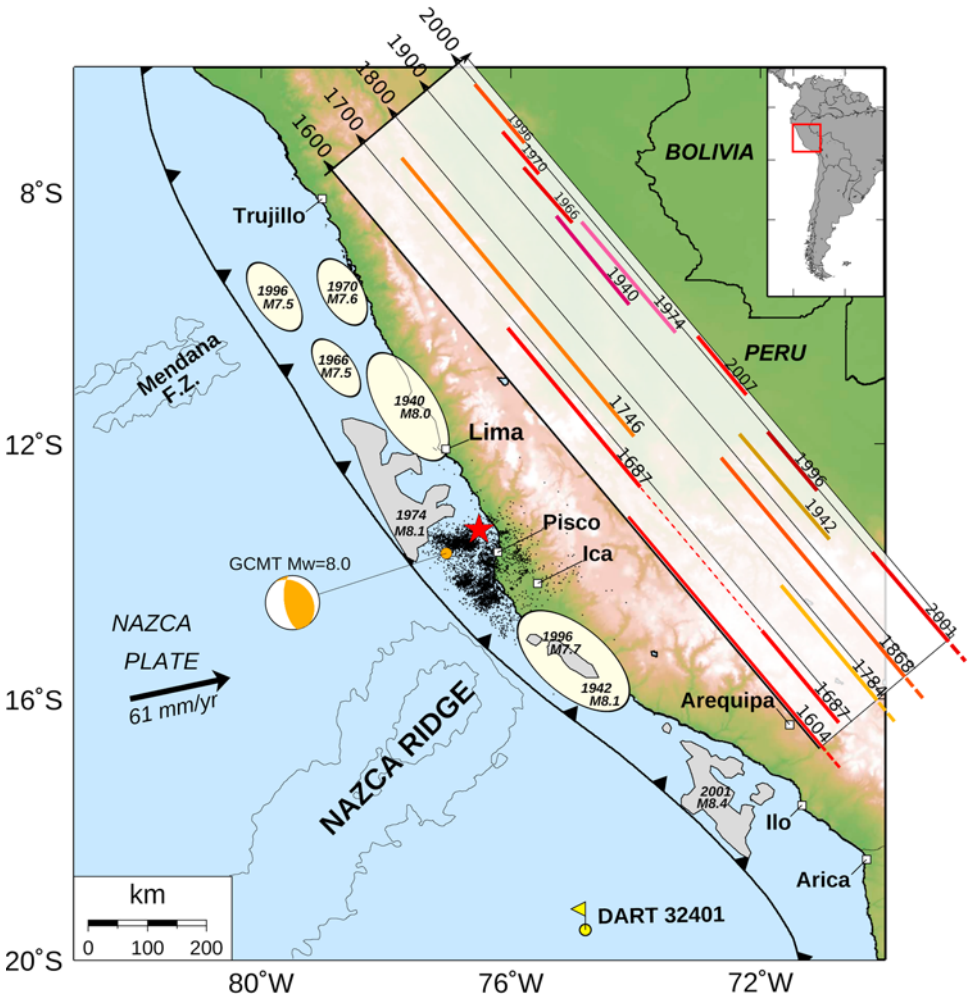

Figure 1. Distribution of recent large interplate earthquakes (light yellow ellipses) in central and southern Peru. Approximate rupture areas for 1974, 1996, and 2001 (grey polygons) from *Langer and Spence* [1995] and *Pritchard et al.* [2007]. Areas of representative ellipses for events without detailed models are derived from scaling relationships [*Wells and Coppersmith*, 1994]. A graph of the large interplate earthquakes since 1604 shows their distribution in time as a function of their along trench extent (adapted from *Dorbath et al.* [1990] for events prior to 1996). NEIC Epicenter and GCMT centroid of the 2007 Pisco earthquake are indicated by the red star and an orange circle, respectively (http://earthquake.usgs.gov/ and http://www.globalcmt.org/). Small black dots indicate aftershocks during the 45 days period following the main shock recorded by a local network of stations. Representative bathymetric contours are shown for the Nazca ridge and the Mendana fault zone. The boundary between the Nazca and the South American plates is shown as a black barbed line, with the relative velocity between the two plates indicated by the arrow [*Norabuena et al.*, 1998]. Location of the Chilean tsunameter used for the tsunami alert is indicated by the yellow symbol.

~200 km to the north. The along strike variation in coastline position is a particularly interesting feature to compare with the rupture area of the 2007 earthquake given that the coastline is generally observed to correlate with the downdip extent of the seismogenic zone [*Ruff and Tichelaar*, 1996]. In addition to providing the most accurate source model of the 2007 Pisco earthquake, our study therefore also aims at illucidating on the seismic behavior of the subduction zone and any relation to the Nazca ridge, and the geometry of the coastline.

[3] Extensive global teleseismic data is available to constrain the rupture characteristics of the 2007 earthquake. These data primarily constrain the chronology of the rupture and are only crudely sensitive to the spatial variations in slip. Teleseismic data is complemented by geodetic observations, such as ground displacement measured from satellite Interferometric Synthetic Aperture Radar (InSAR) can provide strong constraints on the spatial distribution of slip. A number of preliminary finite source models of the 2007 Pisco earthquake have been derived from the inversion of teleseismic and InSAR data [*Sladen et al.*, 2008; *Pritchard and Fielding*, 2008; *Motagh et al.*, 2008; *Biggs et al.*, 2009; C. Ji and Y. Zeng, Preliminary result of the Aug 15, 2007 M_w 8.0 coast of central Peru earthquake, 2007, available at http://earthquake.usgs.gov/eqcenter/eqinthenews/2007/us2007gbcv/; A. O. Konca, Caltech preliminary result

07/08/15 (M_w 8.0), Peru earthquake, 2007, available at http://tectonics.caltech.edu/slip_history/2007_peru/pisco.html; M. Vallée, Earthquakes analysis: M_w = 7.9 07/08/15 Peru earthquake, 2007, available at http://geoazur.oca.eu/spip.php?article107; Y. Yagi, 2007 August 16 off Peru giant earthquake (in Japanese), Tsukuba University, 2007, available at http://iisee.kenken.go.jp/special/20070815peru.htm; Y. Yamanaka, NGY seismological note n°3: August 15 Peru earthquake, 2007, available at http://www.seis.nagoya-u.ac.jp/sanchu/Seismo_Note/2007/NGY3.html]. These previous studies have come up with somewhat different models. Most seismic inversion favor a compound source consisting of two subevents, about 60 s apart (Ji and Zeng, online report, 2007; Konca, online report, 2007; Vallée, online report, 2007; Yagi, online report, 2007; Yamanaka, online report, 2007) and suggest an unusually slow rupture of less than 1.5 km. Such slow rupture is typical of tsunami earthquakes [*Kanamori*, 1972], although this particular event is not classified as such given that the moment magnitude and surface waves magnitude are equal. Also previous studies suggest that the pattern of deformation of the coast measured from InSAR would be consistent with a single slip patch rather than two distinct subevents [*Pritchard and Fielding*, 2008; *Biggs et al.*, 2009]. In addition, the proposed sources have been found to be inconsistent with tsunami observations, in particular the large runups reported south of the Paracas Peninsula [*Fritz et al.*, 2008; Directorate of Hydrography and Navigation, Post tsunami report, 2007, available at http://www.dhn.mil.pe/]. Here, we use InSAR and teleseismic data, as well as tsunami waveforms recorded by deep ocean pressure sensors, field observations of coastal uplift and subsidence and of runup to develop and test a refined model of the spatiotemporal history of slip during the earthquake.

[4] We begin with an overview of some characteristics of the 2007 Pisco earthquake and of the seismotectonic setting. We next present the data set assembled for the purpose of this study, the methods used to analyze and model these data and the modeling results. Finally we compare our source model with a local catalog of aftershocks and discuss general seismotectonic implications of the study.

2. The 2007 Pisco Earthquake and Its Seismotectonic Setting

[5] The relatively long record of historical earthquakes (Figure 1), dating back to the beginning of Spanish colonization in the 16th century [*Dorbath et al.*, 1990], Peru provides important constraints on our understanding of the seismic cycle and the salient parameters controlling characteristics of earthquake rupture. In the region of central Peru, historical records suggest that the last great earthquake (estimated to be a M_w 8.5 to 9.0) occurred in 1746 [*Dorbath et al.*, 1990], and was followed by almost two centuries of quiescence (Figure 1). The most recent event on the northwestern side of the Nazca ridge is the 1974 M_w 8.0 Lima earthquake [*Okal*, 1992]. On the other side of the ridge, the most recent large earthquakes occurred in the period 1942–1996. Detailed analyses of the M_w 7.7 1996 earthquake [*Salichon et al.*, 2003; *Pritchard et al.*, 2007] and a reassessment of the M_w 8.0 1942 earthquake [*Okal and Newman*, 2001] suggest that both events probably ruptured just inland of the coast. Although macroseismic data (aftershocks and isointensity contours) suggest that the 1942 rupture may have extended further south [*Sennson and Beck*, 1996], the 1942 and 1996 ruptures seem to have substantially overlapped and stopped on the southern side of the ridge [*Salichon et al.*, 2003, and references therein]. Thus, it is likely that the flanks of the Nazca ridge were left unbroken by the 1974, 1942, and 1996 events. The region of the megathrust where the Nazca Ridge impinges on the South American Plate represents a segment of the megathrust that has had no significant earthquakes in the recent past. While some portions of this segment are believed to have experienced earthquakes in the distant past, it is not clear the extent to which the central portion of the ridge is in fact seismically active [*Beck and Nishenko*, 1990; *Langer and Spence*, 1995; *Sennson and Beck*, 1996]. The 2007 Pisco earthquake occurred in the northwestern portion of this segment.

[6] This earthquake caused severe damage to the coastal city of Pisco (with a modified Mercalli intensity of VII to VIII) and the surrounding region (Earthquake Engineering Research Institute, Reconnaissance report, 2007, http://www.eeri.org/lfe/peru_coast.html) [*Tavera and Bernal*, 2008], resulting in more than 500 deaths. The earthquake initiated at 23:40:57 UTC (18:40 local time) about 20 km offshore of Pisco (−76.51°E, −13.35°N), at an approximate depth of 39 km (http://earthquake.usgs.gov). The Global Centroid Moment Tensor (GCMT; available at http://www.globalcmt.org) solution is located W–SW of the U.S. Geological Survey (USGS) epicenter and suggests that the rupture occurred along the megathrust with a seismic moment 1.1e + 20 N.m (M_w 8.0).

[7] The earthquake-induced seafloor displacements triggered a tsunami that partially inundated the low-lying city of Pisco (which has an average elevation less than 10 m a.s.l.). A peak runup of 10 m and a maximum inundation distance of 2 km, were reported on the south side of the isthmus connecting the Paracas peninsula (Figure 1) to the mainland [*Fritz et al.*, 2008; Directorate of Hydrography and Navigation, online report, 2007]. Runup amplitudes reached 4 m, 150 km north of the epicenter in Callao (Lima's harbor).

3. Data

3.1. Teleseismic Data

[8] We selected broadband records optimally distributed in azimuth, and all located at teleseismic distance. We considered stations located between 30° and 90° of azimuthal distance, and retrieved the records from the IRIS Global Seismic Network (GSN). Of the initial pool of available records, 22 P wave and 15 SH wave broadband records were selected to provide a good azimuthal coverage (Figure 2). For the azimuths with a great density of stations (California for instance), only records showing coherent and clear phases identified in most of the neighboring records, were retained. In spite of the low density of seismic stations in the Pacific, the final azimuthal distribution of records is satisfactory in the 200°–320° range, and excellent in the other directions. We adopt the weighting of the records to these variations, and because of their lower reliability in timing, the weight on the SH waves is taken as half of the P waves. All body waves are integrated to displacement, and manually picked before bandpass filtering from 1.5 s (P waves) and 3 s (SH waves) to 200 s. Independent of any modeling,

Figure 2. Squares and triangles give the position of the teleseismic stations for which P or P and SH waves have been processed and used for the inversion. Concentric circles are shown every 30° of azimuthal distance from the epicenter.

the seismograms suggest 2 subevents which ruptured about 60 s apart (Figure 3).

3.2. InSAR Data

[9] The western coast of Peru is not always an ideal setting for SAR interferometry, as there is frequently interferometric decorrelation caused by lakes and snow cover, and/or strong topographically correlated path delays due to changes in tropospheric water vapor content. In the coastal plains, migrating sand dunes are also a major cause of decorrelation. From the different satellite images available we generated six interferograms (Table 1), one ERS-2 and two wide-swath Envisat pairs from the European Space Agency (ESA), and three Advanced Land Observation Satellite (ALOS) images obtained by the Japanese Space Agency (JAXA), all providing different viewing geometries (i.e., components of the displacement fields) and spatial extents (Figure 4). We preferentially chose interferograms with short time spans and relatively small perpendicular baselines. Some data was not included in our analysis like, for instance, some Envisat interferograms with 4 years time spans [*Pritchard and Fielding*, 2008].

[10] The Japanese ALOS-Phased Array Type L-Band Synthetic Aperture Radar (PALSAR) sensor provides images at L band frequency (23.6 cm wavelength) is less sensitive to small scatterers such as vegetation [*Miyagi et al.*, 2007], and therefore maintains correlation for longer time spans. The three ascending ALOS interferograms align with the coastline, and correspond to adjacent tracks (109, 110 and 111) in the range direction. The pairs of images were acquired a maximum of two months before, and six weeks after the event; the master image of track 111, which borders the coastline and sample the area of maximum deformation, was taken only 12 days after the earthquake, so the derived interferogram probably includes little post seismic signal (Figure 5). Two Envisat interferograms, with ascending and descending orbits, were processed in wide swath mode (also called ScanSAR) which allows coverage of most of the deformation field, from the high amplitudes along the coast to the long and low-amplitude signal extending across the Andes; the study of *Motagh et al.* [2008] relies solely on these wide swath data. Finally, one ascending ERS-2 image mode interferogram (track 447), centered on the area of maximum deformation, was also considered as it was taken only 2 days after the event.

[11] With the exception of the Envisat wide swath images which were processed using the commercial SARSCAPE

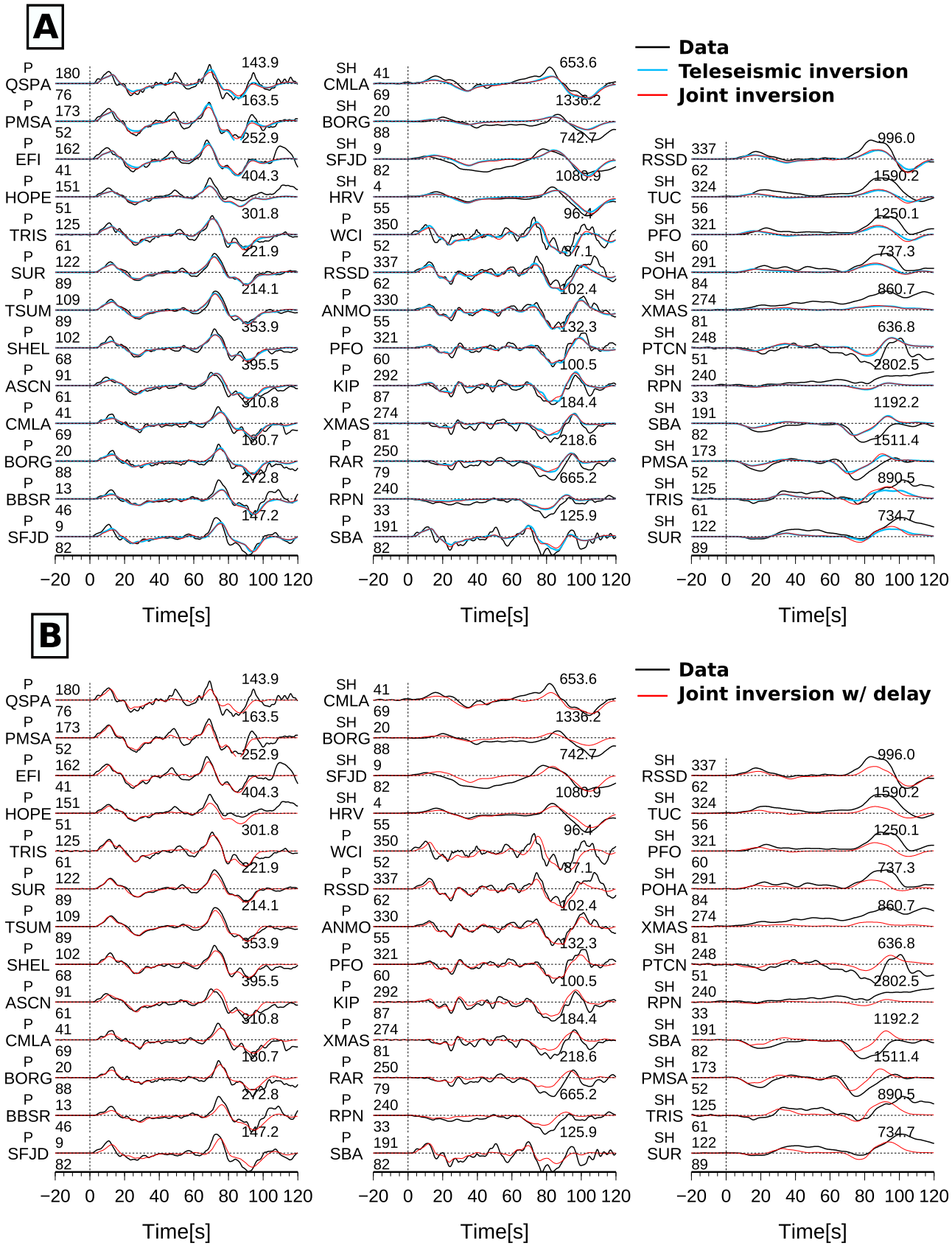
A
Data
Teleseismic inversion
Joint inversion
P QSPA 180 76 143.9 163.5
P PMSA 173 52 252.9
P EFI 162 41 404.3
P HOPE 151 51 301.8
P TRIS 125 61 221.9
P SUR 122 89 214.1
P TSUM 109 89 353.9
P SHEL 102 68 395.5
P ASCN 91 61 310.8
P CMLA 41 69 180.7
P BORG 20 88 272.8
P BBSR 13 46 147.2
P SFJD 9 82
SH CMLA 41 69 653.6 1336.2
SH BORG 20 88 742.7
SH SFJD 9 82 1080.9
SH HRV 4 55 96.4
P WCI 350 52 87.1
P RSSD 337 62 102.4
P ANMO 330 55 132.3
P PFO 321 60 100.5
P KIP 292 87 184.4
P XMAS 274 81 218.6
P RAR 250 79 665.2
P RPN 240 33 125.9
P SBA 191 82
SH RSSD 337 62 996.0
SH TUC 324 56 1590.2
SH PFO 321 60 1250.1
SH POHA 291 84 737.3
SH XMAS 274 81 860.7
SH PTCN 248 51 636.8
SH RPN 240 33 2802.5
SH SBA 191 82 1192.2
SH PMSA 173 52 1511.4
SH TRIS 125 61 890.5
SH SUR 122 89 734.7
−20 0 20 40 60 80 100 120
Time[s]
B
Data
Joint inversion w/ delay
P QSPA 180 76 143.9 163.5
P PMSA 173 52 252.9
P EFI 162 41 404.3
P HOPE 151 51 301.8
P TRIS 125 61 221.9
P SUR 122 89 214.1
P TSUM 109 89 353.9
P SHEL 102 68 395.5
P ASCN 91 61 310.8
P CMLA 41 69 180.7
P BORG 20 88 272.8
P BBSR 13 46 147.2
P SFJD 9 82
SH CMLA 41 69 653.6 1336.2
SH BORG 20 88 742.7
SH SFJD 9 82 1080.9
SH HRV 4 55 96.4
P WCI 350 52 87.1
P RSSD 337 62 102.4
P ANMO 330 55 132.3
P PFO 321 60 100.5
P KIP 292 87 184.4
P XMAS 274 81 218.6
P RAR 250 79 665.2
P RPN 240 33 125.9
P SBA 191 82
SH RSSD 337 62 996.0
SH TUC 324 56 1590.2
SH PFO 321 60 1250.1
SH POHA 291 84 737.3
SH XMAS 274 81 860.7
SH PTCN 248 51 636.8
SH RPN 240 33 2802.5
SH SBA 191 82 1192.2
SH PMSA 173 52 1511.4
SH TRIS 125 61 890.5
SH SUR 122 89 734.7
−20 0 20 40 60 80 100 120
Time[s]

Figure 3

Table 1. List of the InSAR Tracks Used in This Study

Satellite	Track	Orbit Direction	Date of Slave Image	Date of Master Image	Frame Numbers	Perpendicular Baseline (m)
ALOS	111	Ascending	12 Jul 2007	27 Aug 2007	6890, 6900, 6910, 6920	30
ALOS	110	Ascending	10 Aug 2007	25 Sep 2007	6880, 6890, 6900, 6910, 6920	100
ALOS	109	Ascending	24 Jul 2007	8 Sep 2007	6890, 6900, 6910, 6920, 6930	160
Envisat wide swath	447	Ascending	23 Feb 2007	21 Sep 2007	6948	1
Envisat wide swath	311	Descending	5 Dec 2006	20 Nov 2007	3852	48
ERS	447	Ascending	28 Jul 2006	17 Aug 2007	6921, 6903, 6885	190

software, all the interferograms were created using ROI_PAC [*Rosen et al.*, 2004]. We use the 90 m resolution STRM digital elevation model [*Farr et al.*, 2007] to remove the effect of topography. Baselines for the ALOS and ERS-2 interferograms were also reestimated by first removing a preliminary coseismic source model. Lastly, the interferograms were all sub sampled using the method of *Lohman and Simons* [2005] which efficiently reduces the number of data points used in the inversion, while preserving the information contained in the original interferograms at all relevant scales: this final step is mandatory to limit the time of the inversion.

3.3. Tsunami Waveforms

[12] Tsunameters (real-time seafloor bottom pressure recorders) are deployed in open ocean to monitor subduction zones. As most of the energy associated with tsunamis is radiated perpendicular to the coastline, the tsunameter records tend to better sample the tsunami waves than do tide gauges. More importantly, nonlinear coastal effects do not affect tsunameter records. The total potential of those records to resolve the fine details of the earthquake source remains to be explored, but they are supposedly superior to the already informative and useful tide gauges [e.g., *Fujii and Satake*, 2006]. The DART (Deep-ocean Assessment and Reporting of Tsunamis) buoy system, is a network of tsunameters, used for tsunami warning. This network was rapidly expanded in the aftermath of the great Sumatra-Andaman 2004 earthquake (M_w 9.1) and now covers most of the very active subduction zones (39 stations as of March 2008).

[13] The tsunami from the Pisco earthquake was recorded at several tsunameters in the Pacific (Figure 6). This was the sixth large event to be analyzed by the NOAA tsunami warning system, and the open ocean data successfully contributed to the rapid and accurate estimate of the maximum tsunami amplitudes along the considered Pacific coastlines [*Wei et al.*, 2008]. The only flaw though in the tsunami forecast was a systematic 12 min delay in the expected arrival times whose origin had not been clearly determined [*Wei et al.*, 2008].

[14] For the 2007 Pisco tsunami, we selected five tsunameter records from the NDBC-NOAA database (http://www.ndbc.noaa.gov/dart.shtml) with clear centimetric waveforms (all tsunameter used for this study have submillimeter sensitivity). Currently, only 1 min tsunameter data are open to the scientific community [*Wei et al.*, 2008]. We filter out long-period tidal effects from each record by estimating and removing independently a best-fitting sinusoidal component. The tsunameter stations we use are distributed in three distinct azimuths (Figure 6), although none of the stations were in the direction of maximum energy (i.e., perpendicular to the fault azimuth). Consistent with its location less than 800 km south of the rupture, the Chilean station 32401 has the largest amplitude record of the event (more than 8 cm peak to peak). The beginning of this record is dominated by the surface wave of the earthquake (the pressure sensor is attached to the sea bottom), with the tsunami signal only rising out of this noise 51 min after the time of the earthquake, and therefore possibly masking any low amplitude leading wave depression. The southeast Hawaiian station 51406 is west and far away from the epicenter (5,300 km), but the tsunami signal still reaches more than 3 cm in amplitude peak to peak. For unknown reasons, the very beginning of the tsunami signal at this site is truncated. However, the first oscillation starts at mean sea level and has the largest amplitude, suggesting that it corresponds to the beginning of the tsunami signal; again, we may be missing a possible leading wave depression. Three other stations are almost aligned in the same northwest azimuth, but recorded different waveforms of more than 2 cm amplitude in the distance range of 2500 to 6900 km.

3.4. Field Observations of Coastal Uplift and Tsunami Runup

[15] Nine days after the earthquake, we started a survey of the coastline from Laguna Grande-Rancherio (20 km south of the Paracas Peninsula) to Tambo de Mora (80 km north of the Paracas Peninsula) to collect evidences of possible coastal vertical motion and evaluate the impact of the tsunami. The level of the tidal oscillations which, in the case of the Pisco area were estimated to be about 40 cm, limited the interpretation of coseismic coastal uplift which was not expected to be much more than one meter. However, at several locations around the isthmus of the Paracas Peninsula, where observations are made more accurate by the shallowly dipping bathymetry, our field team could rely on a collection of photos taken only one year before to support and refine their measurements; those made on the northern border of the Paracas peninsula were later confirmed by Dr. R.Woodman [*Audin and Farber*, 2008] who estimated the amount of the subsidence to less than 15 cm.

Figure 3. (a) Comparison between the observed (black lines) and the predicted teleseismic waveforms computed from the teleseismic-only (blue line) and joint (red line) rupture models. The location of the station is given in Figure 2. The 22 P wave and 15 SH waves are sorted with increasing azimuth angle (number above the beginning of each waveform, number below is the azimuthal distance). Maximum amplitude of the joint inversion seismograms is indicated above the end of each waveform. (b) Comparison between the observed (black lines) and the predicted teleseismic waveforms computed from the joint rupture model with a fast rupture and an imposed 38 s delay (red line).

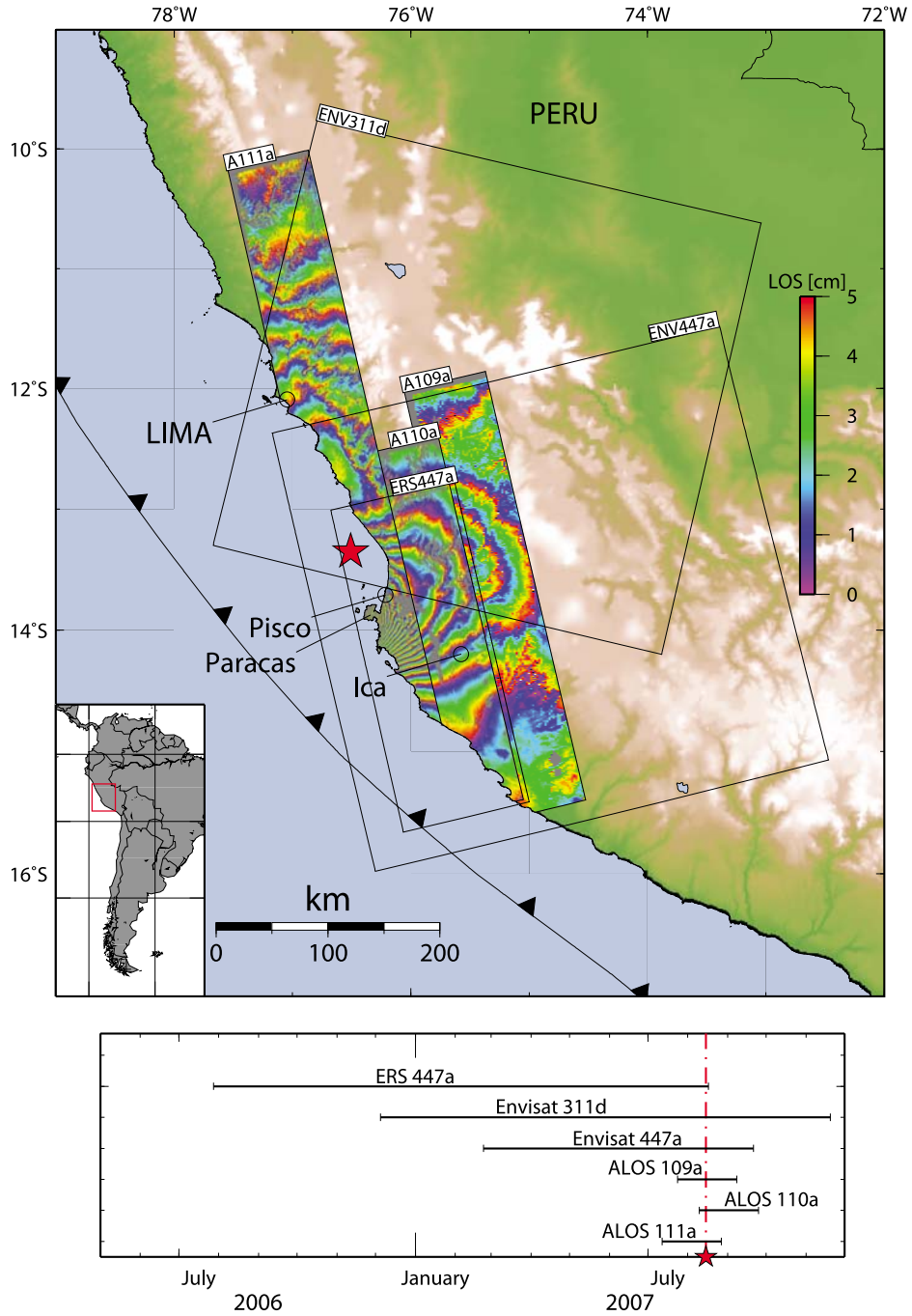

Figure 4. (top) Mosaic of a subset of interferograms used in this study, as well as the spatial extent of the six different interferograms (see auxiliary material for image details). Each interferogram is labeled by: satellite (ALOS, ERS, and Envisat are denoted by A, ERS, and ENV, respectively, at beginning), track number, and direction of orbit (ascending or descending dentoed by a and d, respectively, at end). The red star is the epicenter of the main shock. (bottom) Time span covered by the six InSAR images used in this study. The vertical red line corresponds to the time of the earthquake.

All other surveyed sites did not seem to have experienced any net static vertical motion.

[16] We collected measurements of the tsunami inundation at 41 sites (Figure 7 and auxiliary material).[1] These data are complemented and supported by two other surveys [*Fritz et al.*, 2008; Directorate of Hydrography and Navigation, online report, 2007] which brings the total number of measurements to 114 (Figure 7). The coverage of the coastline is relatively homogeneous from Callao in the North, to the bay of the Independence Island in the South. Along this profile the average runup amplitude is 2 m with a clear broad

[1]Auxiliary materials are available in the HTML. doi:10.1029/2009JB006429.

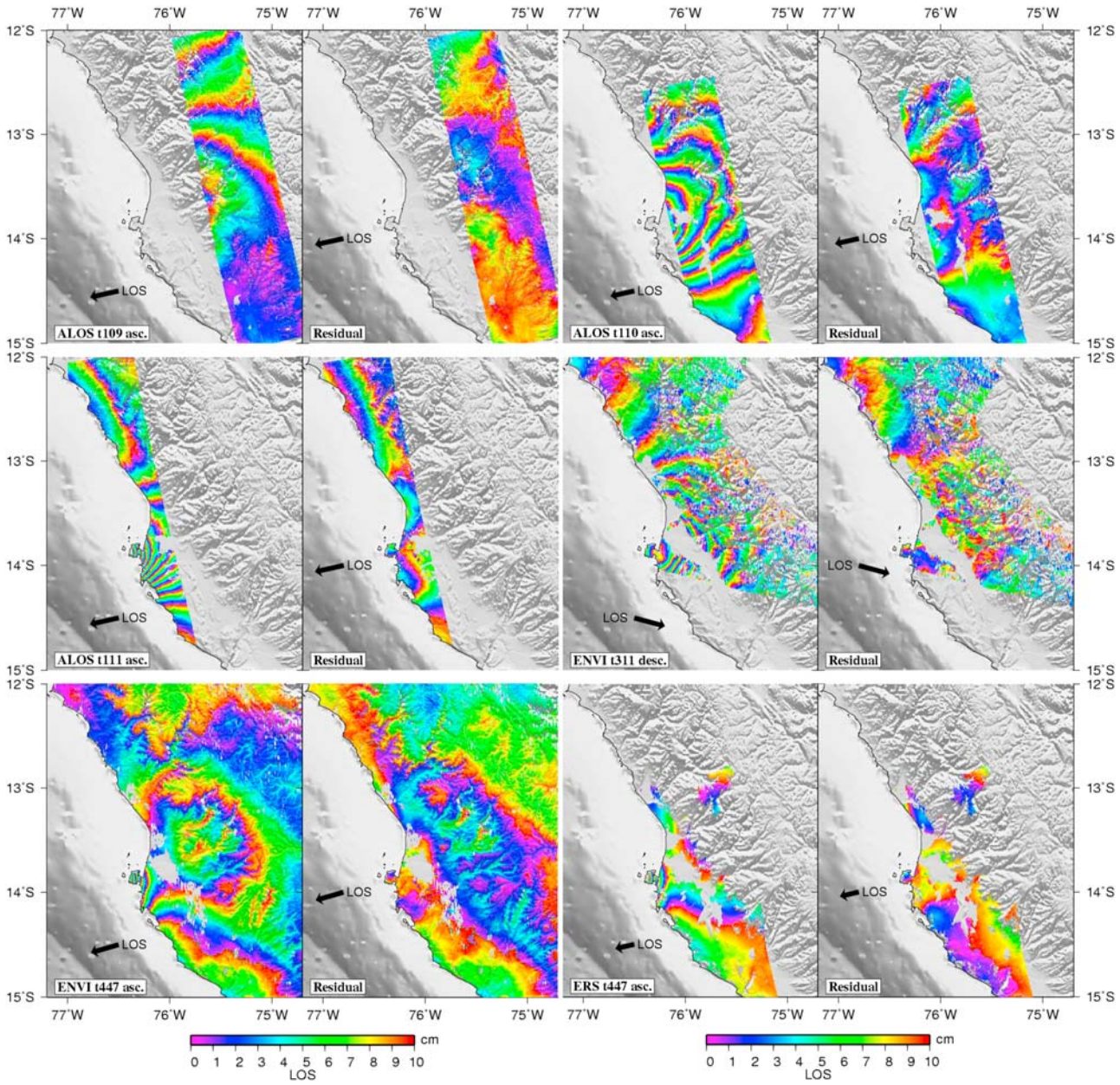

Figure 5. Observed and residual (observed with model and ramp removed) interferograms using results from the joint inversion. All the images are shown with a 10 cm color cycle. The black arrow indicates the surface projection of the ground-to-satellite line-of-sight direction.

peak around the Paracas peninsula with up to 10 m of runup and 2 km of inundation.

4. Methods and Assumptions

4.1. Modeling Strategy

[17] To derive finite source kinematic models, we use the approach developed by *Ji et al.* [2002], which allow the joint inversion of seismic waveforms and coseismic static displacements. Teleseismic and InSAR data provide complementary constraints on the spatiotemporal evolution of the rupture. We first explore the contributions and inherent limitations of each data type before combining them into a single model from a joint inversion. We begin with models constrained only by the InSAR data. We then use these results to develop reasonable bounds on key parameters (e.g., rupture velocity) in the more computationally expensive models that rely only on seismological data. We next compute the tsunami wavefield predicted by our rupture model. The result is compared to the tsunami observations for validation.

4.2. Modeling of InSAR and Seismic Waveforms: Inversion Method

[18] The finite source model is parametrized in terms of a rupture front which propagates along a fault with known prescribed geometry, starting from the hypocenter. The rupture velocity can vary within a range chosen a priori. The risetime function, describing how slip accrues at any particular point on the fault during the rupture, is a simple

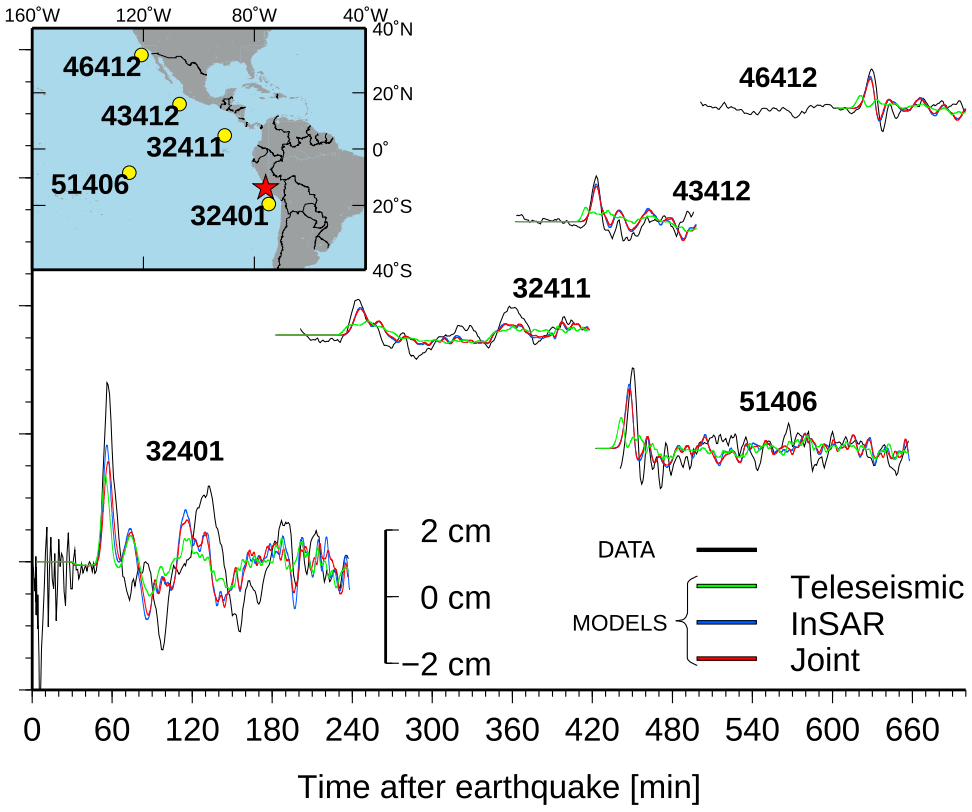

Figure 6. Comparison of the five closest tsunameter records (black) for the Pisco earthquake, with the sea surface perturbations predicted from the joint inversion models. All records are offset to roughly represent their distribution in latitude. They have the same vertical scale and are filtered to remove high-frequency oscillations that are beyond the resolving capacity of our model. The large oscillations at the beginning of the closest station (32401) correspond to seismic surface waves generated by the Pisco earthquake.

quarter wavelength cosine function with adjustable duration. The risetime is allowed to vary within a range of values also chosen a priori. The hypocenter depth is fixed to the value given by USGS-National Earthquake Information Center (NEIC; http://earthquake.usgs.gov).

[19] We compute Green's functions for both the teleseismic and geodetic data assuming a local 1D velocity model derived from the global 3D CRUST2.0 model [*Bassin et al.*, 2000]. The misfit between observed and synthetic waveforms is computed in the wavelet domain using a combination of L1 and L2 norms in order to better capture the entire spectrum of the seismic phases [*Ji et al.*, 2002].

[20] For the InSAR data, we account for variations in line-of-sight directions both between and within each interferogram. Because of uncertainties in satellite orbital parameters, the interferograms can include an apparent displacement gradient that is not related to the effects of the earthquake. We account for this uncertainty in the inversion by subtracting a ramp from the data at each step of the inversion. In the case of the Pisco earthquake, we limit the complexity of this correction to a linear ramp in space. The surface static displacement is computed following *Xie and Yao* [1989], using the 1D structure model also used to model the teleseismic data. The InSAR data are compared with the model predictions using a weighted RMS.

[21] The number of parameters, or unknowns, is controlled by the number of subfaults for which we estimate slip amplitude, rake angle, rupture velocity, and slip duration. Thus, the total number of unknowns is four times the number of subfaults, and can reach several hundred in total. Parameter space is explored using a nonlinear stochastic simulated annealing algorithm [*Ji et al.*, 2002]. Despite the amount of available teleseismic and geodetic data, the inversion requires some form of regularization. In our case, we penalize spatial roughness which is characterized from the spatial Laplacian of the slip distribution, and we also minimize the difference between the final estimated moment and the GCMT value and [*Ji et al.*, 2002]. We empirically set the amount of smoothing such that the main features, here defined as patches with a significant amount of slip distributed over several subfaults, remain compact and smooth while still providing a good fit of the data. The GCMT seismic moment determination, which is used as a reference, can be biased, and in particular by uncertainties in dip angle [*Kanamori and Given*, 1981; *Biggs et al.*, 2009]. However, whereas seismological data have a global sensitivity on the energy released by the rupture, InSAR data usually cover a limited amount of the area of deformation, and therefore have a limited sensitivity to the slip near the trench. This difference of sensitivity is particularly salient in the case of the Pisco earthquake, and suggests that the GCMT moment constraint is less likely to give a wrong answer than an InSAR inversion with no limitation. Finally, our choice is also

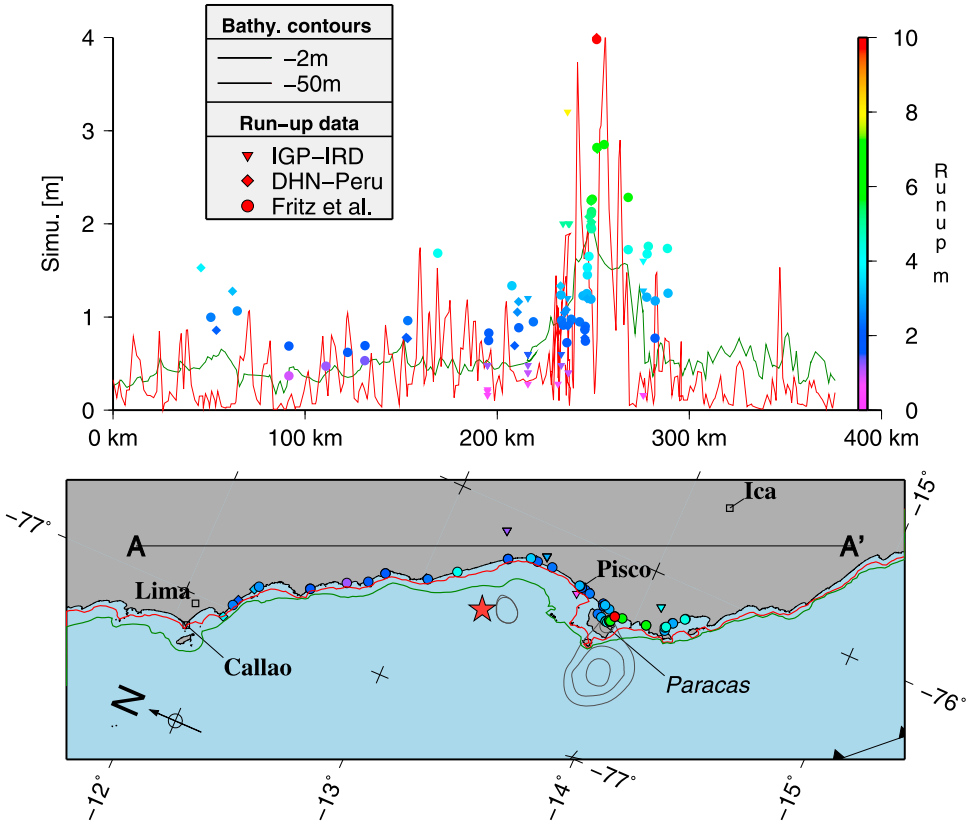

Figure 7. (top) Comparison between the field observations of the tsunami runup amplitudes (inverted triangles, diamonds, and circles) and the nearshore tsunami amplitude for 2 and 50 m depth contours computed using our joint inversion source model (Figure 9c). For comparison, all data presented in Figure 8 (top) are projected along the same A-A′ profile. (bottom) An oblique mercator map view of the runup measurement sites (inverted triangles, diamonds, and circles) and of the 2 and 50 m depth contours (derived from the ETOPO2' bathymetry). The red star is the epicenter location, while the thin black concentric contours correspond to the two asperities of the coseismic rupture.

supported by the recalculated CMT moment of *Biggs et al.* [2009] and *Hébert et al.* [2009], whose value (0.89e21 and 1.07e21 N.m, respectively) are almost identical to the GCMT (1.1e21 N.m), despite significant changes in the dip angle.

4.3. Fault Geometry and Epicenter

[22] We build a simple fault geometry consistent with the epicenter location and 39 km hypocentral depth determined by the USGS-NEIC (http://earthquake.usgs.gov). It consists of 3 planes with progressively increasing dip angle (6°, 20° and 30°) that mimics the changes of curvature of the down going plate (inset in Figure 8a). The planar fault segments strike parallel to the trench (318°N); a value which is only 3° different from the GCMT solution (321°N). The model takes into account the position of the trench, and constraints on the shallow fault portion derived from seismic profiles [*Krabbenhoft et al.*, 2004]. We also consider the ISC catalog, the aftershock catalog described hereafter and the 3D model for the geometry of the top of the subducted Nazca plate derived from a database of independent geophysical information [*Tassara et al.*, 2006, and references therein].

[23] Although we tried to develop a comprehensive model of the fault geometry, it is still possible that the dip angles of our model be wrong by a few degrees. However, intuitively, we know that the static data control the surface location of the slip patches. Thus, a change in dip should not affect much the distribution of slip on the fault plane, but would rather slightly modulate the spatial extent and amplitude of the slip patches.

[24] While a previous study had pointed to a possible lateral variation of the shallow portion of the plate interface from the analysis of the aftershock distribution of the 1974 earthquake [*Hartzell and Langer*, 1993; *Langer and Spence*, 1995], we do not identify any evidence for a similar lateral variation in the data set considered here. However, our simple fault geometry still remains compatible with the relocated earthquakes catalog of *Hartzell and Langer* [1993]. Our fault model is similar to that of *Pritchard and Fielding* [2008], who also used 4 planar subfaults, but considered a narrower range of dip angles (11–25°), and that of *Motagh et al.* [2008].

5. Inversion Results

5.1. InSAR-Only Inversion

[25] We begin by inverting for the distribution of total fault slip using the six radar interferograms (Figure 4). As aforementioned, we test different values of the smoothing

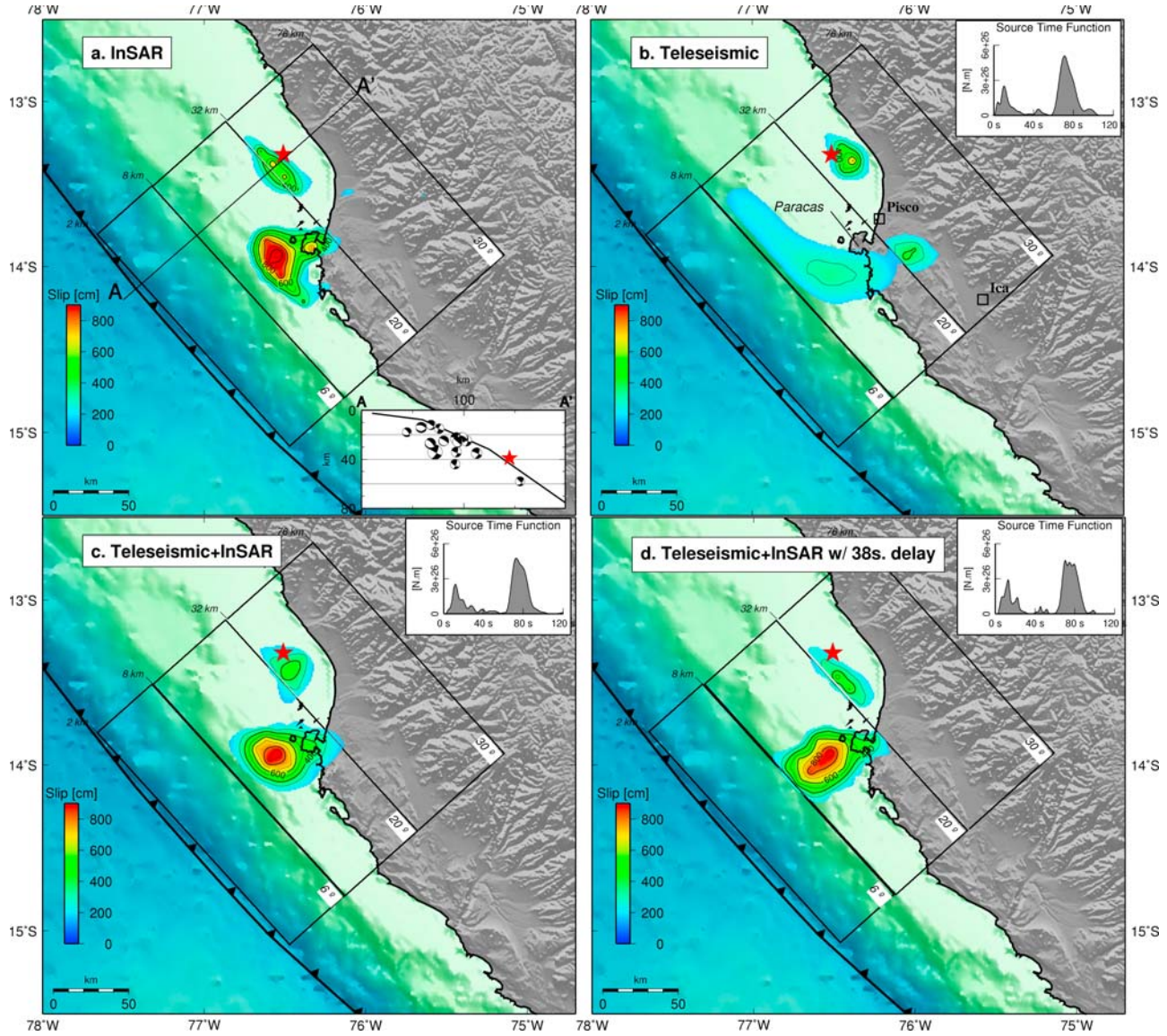

Figure 8. Surface projection of models constrained using different sets of observations: (a) InSAR, (b) teleseismic, (c) teleseismic plus InSAR, and (d) teleseismic plus InSAR with 38 s delay. To highlight the most robust features, we only show regions with inferred slip greater than 2 m, with contours every 1 m. For models using teleseismic data (Figures 9a–9c), the inset shows the estimated source time function. The red star locates the epicenter as located by USGS-NEIC. The large rectangles represent the model fault planes, with assumed dip angles and depths for each fault segment indicated on the eastern and western sides, respectively. Inset of Figure 3a is a cross-section view of the fault model used for the inversion, with the focal mechanism of GCMT catalog. Bathymetry and topography are taken from the ETOPO2 and GTOPO30 databases, respectively.

and select the largest value which can still provide a good fit to the data (Figure 9).

[26] From the inversion, we infer two patches of slip, one close to the epicenter location, and a second larger one reaching 11 m and centered just offshore the Paracas peninsula (Figure 8a). The residuals associated to this solution (section A1) are, on average, limited to one or two fringes and frequently correlate with topography, implying that they are most likely due to propagation delays accrued in the troposphere. We checked that the fit of the data could not be improved by a fault geometry extended further North or South, and this interpretation is also supported by the tsunami and aftershock data analyzed in section 5.2. Finally, we know from three months of GPS observations following the earthquake that the contribution of postseismic deformation should be less than 10% of the coseismic or less than 2 fringes on the inverted InSAR images (H. Perfettini et al., Aseismic and seismic slip on the Megathrust offshore southern Peru revealed by geodetic strain before and after the M_w 8.0, 2007 Pisco earthquake, submitted to *Nature*, 2009). Thus, the small residuals, combined with the simplicity of the slip distribution, and the fact that the first asperity is located where USGS-NEIC places the epicenter suggest that our inferred slip distribution is reasonable. As

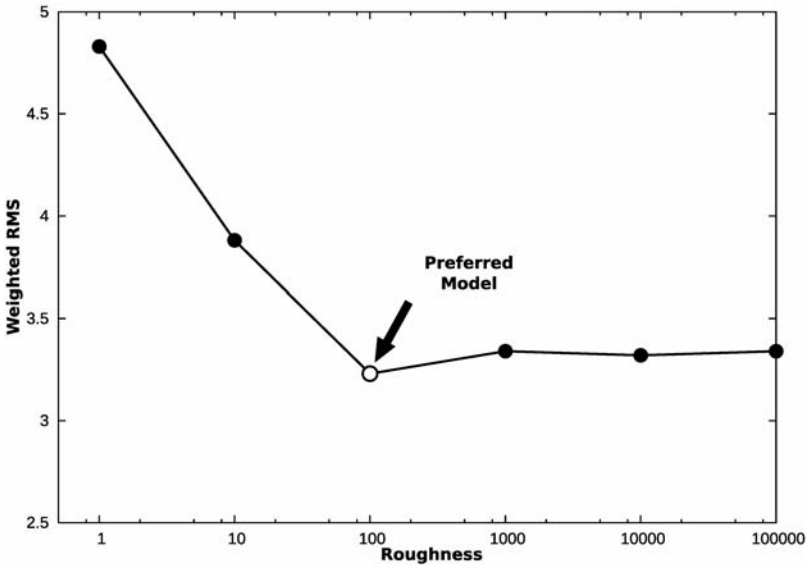

Figure 9. Plot of the weighted RMS of the InSAR-only inversion as a function of the roughness (defined as the inverse of the smoothing factor). The preferred model is indicated by the open dot.

expected from the seismic moment constraint, the inferred value (1.2e21 N.m) is very close to the GCMT value (1.1e21 N.m).

[27] The inferred linear ramp correction for each interferogram (section A1) varies significantly between the image pairs, from negligible on the wide swath Envisat data, to a maximum correction of 20 cm along range for the ALOS track 111 interferogram. The very small correction of the Envisat data is consistent with the expected accuracy of the satellite orbits and the large spatial dimension of the images, which extend to areas with no deformation, and therefore allow more reliable estimation of any biases.

[28] Our solution for the distribution of total fault slip is similar to the InSAR-only model of *Pritchard and Fielding* [2008], although their slip distribution is dominated by the large asperity offshore the peninsula, with only a tail of lower slip extending to the epicentral region. Inversions performed with a larger amount of smoothing, and less moment damping, result in solutions that are even closer to those given by *Pritchard and Fielding* [2008], *Motagh et al.* [2008], and *Biggs et al.* [2009], but do not completely reveal the two slip patches (section A2). Also, the updip extension of the models of *Motagh et al.* [2008] and *Biggs et al.* [2009], in an area where InSAR data has a poor resolution, is probably related to the absence of moment constraint, as the total moment of their solutions is higher than the GCMT value and does not include the epicentral patch.

5.2. Teleseismic-Only Inversion

[29] The InSAR-only inversions permit us to reduce the a priori range of values used in the more computationally intensive inversion of seismograms. We define a narrow range of rupture velocities such that the location of the asperities remains compatible with the InSAR-only model. For the Pisco earthquake, this strategy can be applied fairly easily as the two slip patches of the InSAR inversion correspond to two clear pulses in the teleseismic records (Figure 3). Also, residents in Lima reported two distinct episodes of shaking, separated one from the other by about a minute [*Biggs et al.*, 2009], which is consistent with those two teleseismic pulses. Given that the 60 km separation between the two slip patches of the InSAR-only solution corresponds to a 60 seconds delay in the seismic records, the average rupture velocity has to be around 1 km/s. Thus, for the inversion of the teleseismic data, we limited the rupture velocities to lie between 0.8 to 1.2 km/s. More complex scenarios for the rupture velocity, i.e., combinations of faster and slower rupture velocities, perhaps even stops, could also be considered, an issue that we address further in the discussion.

[30] As expected from the teleseismic waveforms, the slip model inferred from the inversion of only teleseismic data consists of two very distinct asperities, one at the epicenter and a second larger one with most of its energy centered offshore of the Paracas peninsula (Figure 8b). We find a good fit to the observed waveforms (Figure 3) that is comparable to previous teleseismic-only solutions of this earthquake [*Sladen et al.*, 2008; *Pritchard and Fielding*, 2008; Ji and Zeng, online report, 2007; Konca, online report, 2007; Vallée, online report, 2007; Yagi, online report, 2007; Yamanaka, online report, 2007]. The solution of *Biggs et al.* [2009] differs significantly from all the other solutions: the rough rupture history has most of its slip concentrated near the hypocenter, which is at odds with the relatively robust InSAR solution. The differences in the *Biggs et al.* [2009] solution are attributed to a limited amount of regularization and the absence of a healing front in their rupture model. The lack of healing front implies that each area of the fault plane can rupture several times, and in different directions. While we cannot exclude this type of complexity, our model indicates that it is not required by the data. In our teleseismic-only model, the second asperity is not as well focused relative to that in the InSAR-only solution, being smeared along an arc corresponding to the 60 s isochron. This smearing illustrates the lower spatial resolution of the teleseismic inversion, and was already detectable in the contin-

uous teleseismic solutions published online right after the event (Ji and Zeng, online report, 2007; Konca, online report, 2007; Vallée, online report, 2007; Yagi, online report, 2007; Yamanaka, online report, 2007) which all exhibit the same behavior. Our teleseismic-only model differs from those just cited in the inferred smaller distance between the epicenter and the main asperity, a direct consequence of imposing a slow average rupture velocity. In contrast to the InSAR-only inversion, the teleseismic only inversions are highly sensitive to the level of spatial smoothing and moment damping, thus we adopt conservative values (high smoothing and moment damping) to obtain meaningful solutions (i.e., no chaotic slip distribution and reasonable estimates of moment).

5.3. Joint InSAR and Teleseismic Inversions

[31] For the joint inversion of the InSAR and teleseismic data, we explored two possible models. We know from the inversion of InSAR and teleseismic data that the 60 s delay between the ruptures of the two patches with large slip imply a rupture velocity of less than 1.3 km/s given their separation by about 60 km, if it is one rupture. However, it could be two distinct ruptures. One model thus assumes a single rupture with a slow rupture velocity in the range between 0.8 and 1.2 km/s while the other model considers two subevents with conventional rupture velocity (allowed to vary between 2.4 and 2.8 km/s). In the model consisting of two subevents, a delay of 38 s is imposed between the ruptures of the two asperities. In these models, the moment is not constrained, and we apply the amount of smoothing previously determined for the InSAR-only inversion. The current inversion approach is too computationally expensive to allow any systematic search of regularization parameters such as typically provided by cross validation in static-data-only inversions.

[32] As expected from the two previous single data-type inversions, the solution of the joint inversion (Figure 8) shows two distinct patches of slip or asperities. The joint models do not predict slip in the upper segment of the fault plane, an issue to which we return later. The fit to the joint data sets is similar to what was obtained from the independent inversions. The joint models resemble the InSAR-only model without significant degradation of the fits to the seismic data, thereby underscoring the inherent nonuniqueness of teleseismic data. The two joint models also predict nearly identical teleseismic waveforms (Figure 3). One could argue that the fit of the fast rupture model is slightly better, but the difference is small and is likely due to the trade-off between rupture velocity and risetime; the slow rupture model required risetimes an order of magnitude shorter than the fast rupture model to fit the waveforms equally well (Figure 10). Moreover, the improvement in the fit to the seismic waveforms is mostly limited to the first pulse, and does not have any strong impact on the interasperity time sequence.

[33] Two extra small isolated patches that appear in the joint models are not present in the InSAR-only solution (Figure 10). A comparison with the teleseismic-only solution suggests that they are due to the influence of the teleseismic data as they are also located over the same isochron (60 s) as the second asperity. We suspect these small isolated patches are artifacts due to the overly simple seismic velocity structure assumed in this modeling. In any case, we do not expect to resolve such details and thus we do not consider them further. Given the strong similarity between the single data set inversion models (Figure 8), and the minor increase of misfit (Table 2), we do not expect the main features in the total slip model to be strongly altered by small changes in the relative weights between the data sets.

[34] For all three classes of models, the rake angle is fairly constant over the entire fault plane (a sign that the inversion is stable) with an angle around 63°, corresponding to a horizontal convergence direction of N105°, equal to that inferred geodetically [*Norabuena et al.*, 1998]. This event therefore is consistent with the hypothesis that the oblique motion on the Peru megathrust is not partitioned [*Norabuena et al.*, 1998].

6. Consistency of Tsunami Observations and Model Predictions

[35] To model the tsunami, we assume that its initial state fully and instantaneously matches the vertical sea bottom deformation caused by the earthquake, including the vertical component due to horizontal motion of the bathymetry [*Tanioka and Satake*, 1996]. This initial water column perturbation is then propagated using the classical nonlinear shallow water equations, implemented in a finite difference scheme [*Heinrich et al.*, 1998; *Hébert et al.*, 2001]. The propagation model uses the 2′ resolution global ETOPO2v2 bathymetric grid [*Smith and Sandwell*, 1997].

[36] We compare the tsunameter data (Figure 6) with predictions from our three previously presented models (Figure 8). Since the tsunami modeling depends only on the static surface deformation pattern, the InSAR and joint inversion models produce very similar sea surface height perturbations (computed using a 1D model and the method of *Xie and Yao* [1989]), both of which match the observed records. On the other hand, the waveforms produced by the teleseismic-only model lack energy, and phase arrivals are not properly aligned. In particular, at all the stations west or north of the rupture, the initial phase is systematically early suggesting that the slip distribution of the teleseismic data extends too much in those directions. These premature arrivals imply that the source of the earthquake has to be distributed very close to the coastline, and that scenarios of a rupture mainly focused around the hypocenter (teleseismic model of *Biggs et al.* [2009]), or extending close to the trench, as in the model of *Motagh et al.* [2008], are not compatible with those tsunami data. Inversions performed by *Motagh et al.* [2008] indicate that changes in geometry seem to primarily affect amplitude and not the spatial extent. Therefore, we infer that the increased slip updip in their model is most likely the consequence of using only two wide swath Envisat interferograms. These data are sufficient to constrain long wavelengths components of the deformation, but they are probably insufficient to capture the subtle gradient variations near the coast, which help define the distant contour of the source. Without a priori constraint on the total moment of the earthquake, our models also predict slip on the upper shallower portions of the fault. With a moment constraint and perhaps aided by the fortuitous offset of the coastline and the proximity of the high slip patches to the coast, the InSAR-only model appears to predict the Pisco earthquake slip distribution with sufficient fidelity, that it also satisfies the tsunameter data. In general, the tsunameter data remains critical to tightly constrain the updip behavior of a megathrust earthquake.

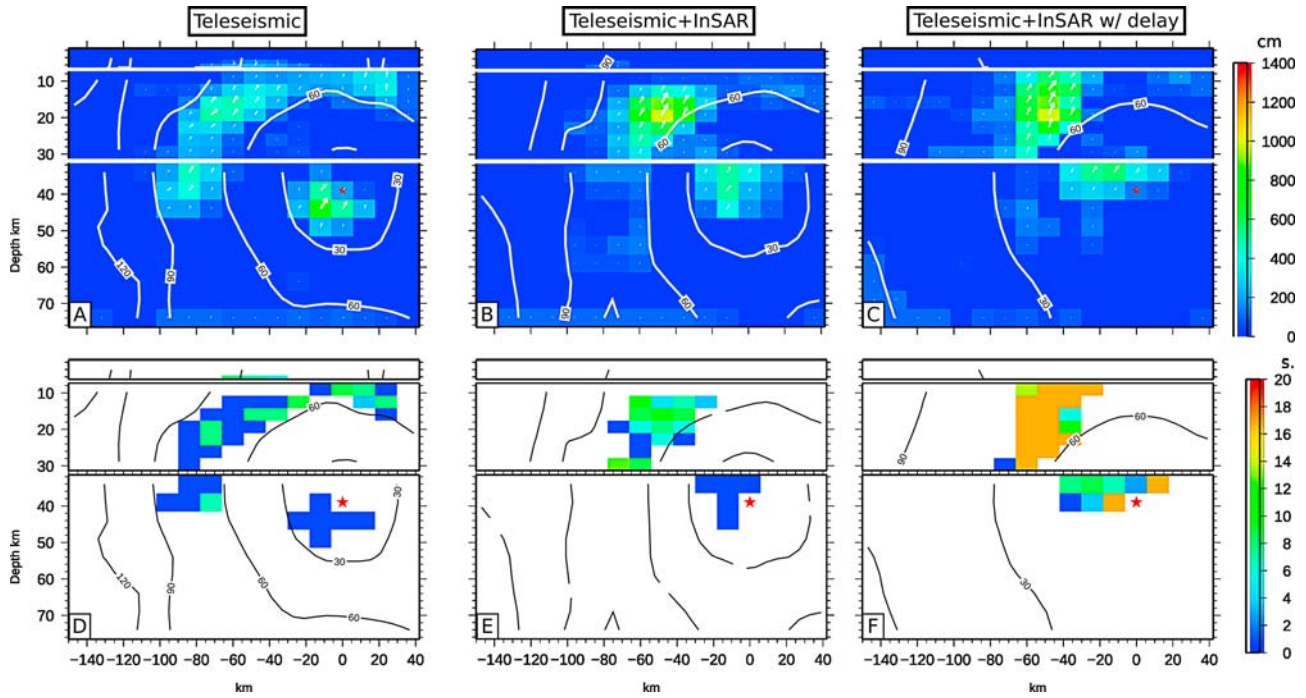

Figure 10. Head-on view of the (a–c) slip and (d–f) risetime distributions on the fault segments obtained from the teleseismic (Figures 10a and 10d), joint inversion of teleseismic and InSAR data using a low rupture velocity (0.8–1.2 km/s; Figures 10b and 10e), or faster rupture velocity (2.4–2.8 km/s) with an imposed 38 s time delay of the rupture front between the two lower segments (Figures 10c and 10f). Color levels correspond to the amount of slip or duration of the risetime on a given subfault, with the direction of slip indicated by the white arrows. On the right hand side, the risetime value is only shown for subfaults that experience more than 200 cm of slip.

[37] The successful tsunami predictions of the InSAR-only and joint models indicate that the origin of the 12 minutes timing error reported in the simulation of the tsunami alert system [*Wei et al.*, 2008], is indeed due to an approximate earthquake model: in comparison with our best slip model, the inversion procedure of the forecasting system mislocated the slip by one fault element (100 km) to the North. This distance is equivalent to 12 min of tsunami propagation in a 2 km deep water layer, as what is found in the area of the main slip patch. We suggest that the mislocation resulted from the use of only station 32401 for the estimate of the source model: although this station is closest to the source, its southeast azimuth does not allow us to unambiguously resolve the extent of the source in the opposite azimuth. This effect was independently confirmed by the source model of *Hébert et al.* [2009], based on tsunameter record 32401, which also predicts a tsunami arriving too early at station 51406, and at the tide gage of the Taiohae Bay (Nuku Hiva Island, Marquesas Archipelago). Therefore, tsunami travel time can only be considered accurate in the azimuths of the stations used to estimate the source, and the future tsunami forecasts would benefit from the inclusion of tsunameters located in various azimuths. Our forward models also suggest that the timing error related to the propagation model is probably below one percent of the travel time in open ocean for this part of Pacific.

[38] While our predicted waveforms match those observed at the more distant stations, they do not match that well the signal recorded by the nearby buoy 32401 (Figure 6). The predicted arrival time at the station is fine, but the amplitude of the first peak is underestimated and the subsequent phases arrive too early. As all those secondary arrivals correspond to early reflections of the initial perturbation on the coastline, this compression of the waveform phases toward the initial peak are likely to be caused by the coarse 2′ bathymetric model which does not accurately reproduce the shallow

Table 2. Misfits Between Observations and Models' Predictions[a]

Model Type	InSAR Data (WRMS in cm)	Teleseismic Data (L1 + L2 Norm of Wavelet Coefficient)	Tsunami Data (WRMS in cm)
InSAR model	3.23 (6.46, 5.59, 0.85, 1.88, 3.66, 0.94)	NA	0.49
Teleseismic model	NA	0.2	0.57
Joint model	4.37 (8.08, 7.14, 1.19, 3.43, 4.99, 1.41)	0.21	0.48
Joint model with delay	4.72 (7.9, 9.1, 1.27, 3.42, 5.28, 1.29)	0.21	0.48

[a]WRMS stands for weighted root mean square and NA stands for not available. For the InSAR data, numbers in parentheses are for each of the individual tracks (ENVI-447a, ENVI-311d, ERS-447a, ALOS-111a, ALOS-110a, ALOS-109a).

coastal areas where the tsunami is expected to slow down. This implies that the section of a tsunameter record used to image the earthquake rupture, like the Pisco earthquake [*Hébert et al.*, 2009], can be extremely limited (less than 60 min) without a detailed model of the coastal bathymetry. The underestimation of the first peak could result from errors in the fault geometry, too much smoothing and moment damping, and from not taking into account the horizontal velocity component of the deformation with sufficient accuracy [*Song et al.*, 2008].

[39] The use of a coarse bathymetric grid does not allow us to predict the precise runup and inundation distances. However, the first-order characteristics of the tsunami impact are controlled by the earthquake slip distribution, and it is possible to compare the general shape of the predicted tsunami amplitudes close to the shore with the distribution of tsunami amplitudes. Using this approach, *Fritz et al.* [2008] showed that, neither a uniform slip model, nor a composite slip model with most of the slip south of the Paracas peninsula (as suggested by the preliminary teleseismic-only models), could explain the coastal distribution of runup amplitudes. We use our joint model (Figure 8c) to compute the profile of tsunami amplitudes along the 2 and 50 meters depth contours (Figure 7). Both profiles predict the shape of the distribution of runup amplitudes and its strong peak near the Paracas peninsula. This comparison confirms the validity of our source model and, given the poor prediction of the simple source models tested by *Fritz et al.* [2008], it also demonstrate the high correlation of the near-field tsunami impact and the slip distribution on the fault. While the 2 meter depth profile predicts the broad peak distribution of runup amplitudes around the Paracas peninsula, it fails to correctly predict other peaks observed further north and toward the harbor of Callao. Thus, for a 2′ resolution bathymetry, switching from a 50 m depth profile to a 2 meter depth profile does not significantly improve the tsunami impact estimations.

6.1. Is the Pisco Earthquake a Tsunami Earthquake?

[40] A limited number of large earthquakes with very slow rupture velocity (<1.5 km/s) have been identified in subduction zones, these include two in northern Peru [*Okal and Newman*, 2001]: the 20 November 1960 earthquake and the Chimbote earthquake of 21 February 1996. These slow rupture events fall into the specific category of so-called tsunami earthquakes [*Kanamori*, 1972] as they tend to produce larger tsunami waves than what is normally expected based on their moment magnitude. The unusual tsunami excitation is thought to be related to their shallow depth, where the surrounding material is less consolidated. As a consequence of the lower rigidity of the medium, the upper plate is more strongly deformed and transmits more energy to the overlying water column [*Fukao*, 1979; *Okal*, 1988]. The low rigidity also causes the rupture to propagate more slowly, and therefore to radiate less high-frequency energy. This later effect explains the difficulty to estimate the true moment of a tsunami earthquake when not taking into account long-period energy, as is the case of local and surface wave magnitudes [*Weinstein and Okal*, 2005]. There is no M_s-M_w magnitude discrepancy for the 2007 Pisco earthquake (the GCMT analysis determined a value of 8.0 for both). More importantly, the forward tsunami simulation from our slip model does not require any modification to match the open ocean records (Figure 6) nor the runup data (Figure 7). These arguments imply that the Pisco earthquake does not fall in the category of tsunami earthquakes, and is indirectly consistent with the conclusion that the rupture did not extend to the trench.

6.2. Comparison of Coseismic Slip and Aftershocks Distribution

[41] The 2007 Pisco earthquake was followed by a strong aftershock activity. Hundreds of aftershocks with magnitude greater than M_L 2.5 were located using a local network of 12 short-period seismometers installed in the Pisco region by the Instituto Geofísico del Perú (IGP). Here, we discuss the first 45 days following the main shock, a period assumed to be largely long enough to identify the final stable patterns of an aftershock sequence [*Das and Henry*, 2003]. During this time period, the catalog recorded more than 4500 events with magnitude M_L ranging from 2.1 to 6.2. Despite using conventional location algorithms, and a network with only partial azimuthal coverage, the alignment of one cluster of aftershocks along the coastline between −13.5°N and −14.5°N (Figure 11) suggests that mislocation errors are sufficiently small to not affect the interpretation of the large-scale patterns. Furthermore, two swarms located updip of the hypocenter and south of the Paracas Peninsula also appear distinctly and at the same location, in both the global NEIC-USGS (http://earthquake.usgs.gov) and ISC catalogs (http://www.isc.ac.uk). The spatial clustering of events obtained with this aftershock catalog is a common feature of the Peruvian margin, and has already been pointed out for several other large megathrust events [*Dewey and Spence*, 1979].

[42] We find a remarkable anticorrelation between the spatial distribution of aftershocks and our inverted slip model (Figure 11), with little aftershock activity in the areas of high slip and a high density of events in the surrounding area. To avoid apparent biases induced by the way the aftershocks are plotted, we computed the normalized probability density function of the catalog using a Gaussian kernel estimator [e.g., *Scott*, 1992] (Figure 11). This continuous representation highlights two areas of high aftershock density, again clearly complementary with the areas of high slip. This observation adds support to the idea that the Pisco earthquakes really consists of two distinct asperities.

[43] This anticorrelation between aftershocks and regions of large coseismic slip has also been observed in a number of studies of other earthquakes. In the context of continental strike-slip faults, the 2004 Parkfield earthquake (M_w 6.0), which occurred along the most instrumented section of the San Andreas fault (California, USA), is probably one of the more robust evidence of the anticorrelation of aftershocks and main slip patches [e.g., *Woessner et al.*, 2006; *Kim and Dreger*, 2008]. The Parkfield event was studied in conjunction with several previous continental earthquakes to show that this anticorrelation is indeed statistically significant [*Woessner et al.*, 2006]. The same observation has been reported for a number of recent subduction earthquakes for which the source models could be constrained from geodetic data. They include the M_w 8.1 Antofagasta earthquake of 1995 [e.g., *Pritchard et al.*, 2002], M_w 8.0 Tokachi-Oki earthquake of 2003 [*Koketsu et al.*, 2004], the M_w 8.7 Nias earthquake of 2005 [*Hsu et al.*, 2006; *Konca et al.*, 2007], or

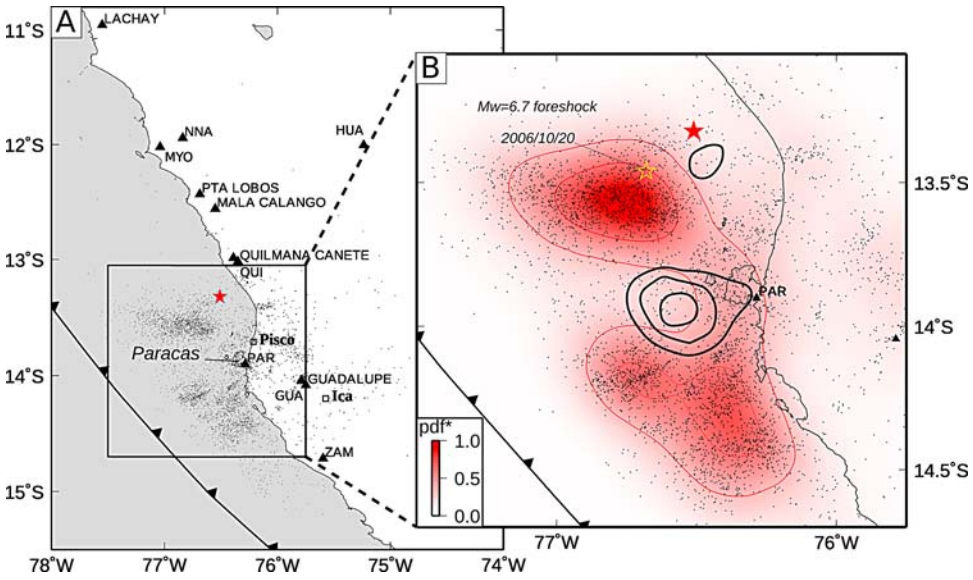

Figure 11. (a) Distribution of aftershocks recorded by a local IGP seismological network (triangles) during the 45 days following the main shock. (b) Zoom on the area of large aftershock activity. A normalized probability density function for this catalog is shown in red color, with thin red contours every 0.3 of a unit. Also indicated are 2 m contours of slip 2 m from the joint inversion (black contours). The red star is the epicenter of the 2007 Pisco main shock, and the yellow star shows the location of the large M_w 6.7 foreshock of 20 October 2006.

the M_w 7.6 Tocopilla earthquake of 2007 [*Delouis et al.*, 2009]. None of these studies show as clear a correlation as the one observed for the 2007 Pisco earthquake: both in terms of the high occurrence of aftershocks in areas of low slip, but also in terms of surrounding the slip patches to create a well delineated quasi-rectangular area limited downdip by the coastline. Our ability to detect these correlations was greatly facilitated by the dense local seismic network that includes stations within the area of aftershocks (e.g., station PAR, in Figure 11).

[44] The paucity of aftershocks downdip of the coseismic slip areas, and their concentration above or to the side of the regions of high coseismic slip, is similar to what was observed for several large recent subduction events such as the 2001 Arequipa, Peru, 2003 Tokachi-Oki, Japan and 2007 Nias, Indonesia earthquakes [*Miyazaki et al.*, 2004; *Perfettini et al.*, 2005; *Hsu et al.*, 2006]. These studies found that aftershocks are collocated with regions of inferred high afterslip, and follow the same temporal evolution as the afterslip. This type of relation suggests that afterslip is driving the generation of the aftershocks surrounding the coseismic rupture [*Perfettini and Avouac*, 2004; Perfettini et al., submitted manuscript, 2009].

6.3. Pisco Earthquake as a Composite of Two Distinct Events

[45] The modeling results do not allow us to uniquely determine whether the source is best represented as a single rupture with slow rupture velocity or by two subevents with usual rupture velocities. The 2007 Pisco earthquake ruptured at a depth range and distance from the coast which are typical of the largest interplate earthquakes of the South American margin (we exclude the previously discussed tsunami earthquakes) and, to our knowledge, none of those previous events had an anomalously slow rupture velocity, that is below 1.5 km/s. Although it can be argued that this is merely the result of unconstrained analysis, it supports the idea that the two slip patches ruptured at standard rupture speeds and were separated by either an area with significantly slower rupture velocity, a quasi-creeping zone, or that the distribution of slip is in fact completely discontinuous, implying that the two high slip patches were distinct events.

[46] The moderate magnitudes reached by the largest aftershocks is another indication that the compound source model is more plausible. The empirical Båth's law [*Båth*, 1965] states that the difference in magnitude between a main shock and its largest aftershock is close to 1.2. In the case of the 2007 Pisco earthquake, the difference between the main shock (M_w 8.0) and the largest aftershock (M_w 6.4, GCMT catalog) is 1.6. One could reconcile these magnitudes with Båth's law by considering the scenario of a main shock made of two distinct events with lower magnitudes. In the joint inversion model, the magnitude inferred for the largest asperity is M_w 7.8, which reduces the difference with the largest aftershock from 1.6 to 1.4. However, the validity of Båth's law is still debated and the value of 1.2 is only a statistical mean [*Console et al.*, 2003, and references therein]. Thus, the difference between the two scenarios is probably too small to use Båth's law as a conclusive argument.

[47] While the possibility of two distinct events eludes the problem of the apparent slow rupture velocity, it poses the question of the mechanisms that could have triggered the second event. This process could either be dynamic, via the propagation of seismic waves, or static, through delayed mechanical stress transfer. In both cases, the 38 s would simply reflect the time it has taken for the second subevent to nucleate in response to static or dynamic triggering by the first event. One could speculate that the rupture barrier

resulted from a zone of low stress inherited from the previous earthquake or creep [*Konca et al.*, 2008]. Alternatively, if the intensity of the aftershock activity is somehow related to a readjustment of stresses on the interface, then the intermediate level of aftershock activity observed in this transition area, intermediate between the very low density of the areas of peak slip, and the high density of aftershock clustering, suggests aseismic creep in the area separating the two seismic asperities. This would be expected if that area was governed by a rate-strengthening friction law [*Perfettini and Avouac*, 2004; *Perfettini and Ampuero*, 2008]. In that case, the 38 s would represent the time it took for the static stress change to reach a high enough level to trigger seismic rupture of the second asperity. Lastly, from detailed inspection of the aftershock catalog, we note the tendency of the northern cluster to align in an almost east–west direction (Figure 11), that is oblique to the trench and the convergence direction; while we do not see any obvious structure in the bathymetry which could explain this alignment, the speculated area of creeping would be in the downdip continuity of this cluster and could indicate a hidden structural relation.

6.4. Coastline Position Reflects the Geometry of the Seismogenic Zone

[48] *Ruff and Tichelaar* [1996] identify a statistically significant correlation between the location of the coastline and the downdip limit of the seismogenic zone. This work, based on the analysis of the aftershock distribution of large circum-Pacific earthquakes, also concludes that ruptures extend on average to a depth of 40 ± 5 km [*Tichelaar and Ruff*, 1993]. *Ruff and Tichelaar* [1996] also point out the correspondence between the coastline and the approximate location of the contact between the subducting plate and the Moho of the overlying plate. Associating the Moho with a rheological transition leads to an explanation for the coincident location of the coastline with the downdip limit of earthquakes, and why earthquake ruptures do not extend much deeper. Two studies on the Sumatran [*Simoes et al.*, 2004; *Singh et al.*, 2008] and Japanese subduction zones [*Suwa et al.*, 2006] found evidence that the transition from the locked fault zone to the creeping zone can extend deeper than the forearc Moho. Numerical modeling on the thermomechanical evolution of subduction zones also suggest that the downdip limit of the frictional deformation may coincide with the coastline [*Fuller et al.*, 2006].

[49] Two elements of the Pisco event allow us to further refine interpretations of the relationship between coastlines and downdip rupture extent. First, the inferred slip distribution is located close to the coast and has been tested against teleseismic data, a large set of InSAR, tsunami, field, and aftershock data, leaving very little space for alternative solutions. Second, the 2007 Pisco earthquake occurs along a markedly sinuous section of coastline: this curvature allows us to go beyond the standard 2D cross-sectional view of subduction zones.

[50] Neither the inverted coseismic slip models (Figures 8c and 8d), nor the distribution of aftershocks (Figure 11) of the Pisco earthquake aligns with the trench. Rather, both strongly deviate updip paralleling the coastline as the rupture propagates southeastward. These observations themselves support the idea of a relationship between the earthquake slip pattern and the coastline. In order to further explore this relationship, we compute the predicted coseismic vertical displacement of the surface (Figure 12). We find a striking anticorrelation between the vertical deformation pattern and topography: uplifted areas are strictly offshore and follow the coastline, whereas the maximum subsidence spreads out behind the peninsula with a maximum subsidence almost coincident with the peninsula. A study using InSAR and teleseismic data found similar results for the 1996 Nazca earthquake [*Salichon et al.*, 2003], but along a section of the margin where the coastline does not show any along strike complexity.

[51] The coincidence of the pivot line (sometimes called hinge line although it is not characterized by any significant bending), with the coastline is supported by the conclusions of a field survey we carried out in the days following the earthquake, and from which we reported no noticeable uplift or subsidence along the shoreline [*Audin et al.*, 2007]. This anticorrelation between the coseismic vertical deformation pattern and topographic relief indicates that, at the scale of a single seismic cycle, the deformation is linked to topography and bathymetry [*Audin et al.*, 2008]. *Ruff and Tichelaar* [1996] propose a simple isostatic model to explain the coincidence of the coastline with the downdip limit of the seismogenic interface. Another, and not necessarily contradictory argument, is provided by the studies of *Wells et al.* [2003] and *Song and Simons* [2003], which have found that the areas of maximum slip during large earthquakes tend to correlate with gravity lows and the associated forearc basins. *Song and Simons* [2003] suggest that gravity lows and forearc basins are located above the parts of the slab interface with relatively low normal tractions but high shear tractions. This association of the gravity lows with regions of high coseismic slip, suggests a relationship between the regions experiencing a seismic cycle (i.e., the classical stick slip behavior) and the long-term evolution of the forearc. For this relationship to hold, there must be net long-term deformation in the forearc induced by having a seismic cycle. This anelastic deformation has to build up during the interseismic period given that the coseismic deformation deduced for the 2007 Pisco earthquake has the wrong polarity to explain topography. The long duration of the interseismic phase also supports the possibility that the medium is not responding is a purely elastic way. While this net deformation is not consistent with what is normally assumed when using an elastic dislocation model where coseismic and interseismic deformations cancel, we expect that the anelastic deformation produced over a single seismic cycle has to be small [*Savage*, 1983; *King et al.*, 1998] and to first order negligible when modeling interseismic geodetic data. This hypothesis is also supported by studies of paleoevents along other subduction zones [*Kelsey et al.*, 2006; *Nelson et al.*, 2008].

[52] Sites along subduction margins where the coseismic and long-term surface deformation patterns can be compared are very rare due to the presence of the oceans. One example though is the study of *Briggs et al.* [2008] on the outer arc island of Nias, Indonesia, which recently experienced a M_w 8.7 earthquake (March 2007). Their measurements of the Holocene uplift rates, and their comparison with the coseismic values revealed dissimilar and nonproportional patterns of deformation. Their result does not seem compatible with our inferences from the 2007 Pisco earthquake. However, we note two major differences between the tectonic contexts of

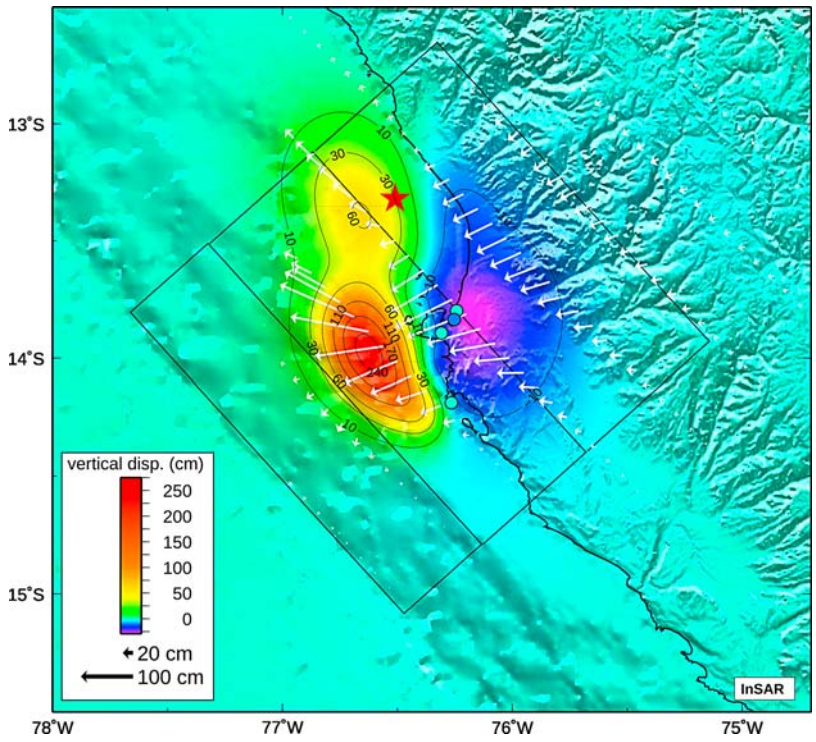

Figure 12. Map of the static surface deformation predicted from the InSAR-only inversion solution. Color represent the vertical component of displacement, while the horizontal motion at the Earth surface is represented by the white arrows. Locations of the most accurate field observations of vertical coastal motion are indicated by the colored dots (blue for subsidence and green for no significant motion). We do not show estimates from field sites that are within errors associated with tidal corrections.

those regions: first, the Peru forearc basin has a large subsidence rate (500 m/m.y. over the past 5 M.y) [*Von Huene and Lallemand*, 1990] while there is no such trend in North Sumatra [*Briggs et al.*, 2008]. Second, Sumatra is an accretionary margin accumulating large amounts of sediments [*Von Huene and Scholl*, 1991], which can greatly influence the distribution of deformation within the wedge [*Fuller et al.*, 2006]. *Ruff and Tichelaar* [1996] also noted this general distinction between continental and oceanic margins in their analysis of the coastline-aftershock correlation. More fundamentally, the *Song and Simons* [2003] results only make sense in the context of a forearc where gravity and bathymetry only reflect presently active processes directly associated with the megathrust. In Sumatra, the offshore islands are not presently uplifting at significant rates [*Briggs et al.*, 2008] and thus are not representative of the present-day deformation field. In sum, the results of the Nias study are probably not applicable to the Peru margin, and the underlying reason might also be the cause for the failure of the gravity-rupture relationship along the margin offshore of central Sumatra [*Grevemeyer and Tiwari*, 2006].

6.5. Long-Term Seismic Behavior of the Megathrust: A Bimodal Behavior With Infrequent Very Large Earthquakes Reaching Close to the Trench

[53] Historical accounts for central Peru (−10°N to −15°N) report two very large events in 1687 and 1746 (Figure 1), with magnitudes close to M 9 [*Dorbath et al.*, 1990]. Subsequently, this stretch of the South American coast has not experienced any major earthquake [*Dorbath et al.*, 1990]. This observation is probably robust as events with magnitude less than M 8 are reported as far back as 1586. After this quiet period, the 1940 North of Lima earthquake marks the return to strong activity, with the 2007 Pisco earthquake being the most recent in a sequence of 6 earthquakes with magnitudes between 7.5 and 8.2: 1940, 1942, 1966, 1974, 1996 and 2007 (Figure 1). These recent earthquakes seem to have ruptured complementary segments that mosaic the rupture areas of the 1687 and 1746 earthquakes [*Dorbath et al.*, 1990].

[54] This bimodal pattern of energy release, either through exceptionally large events (1687 and 1746), or through a sequence of smaller events filling the same area (1940–2007), is analogous to what was observed for the Colombia-Ecuador margin which all ruptured in once in 1906 (M_w 8.8), and then in three stages: 1942 (M_w 7.9), 1958 (M_w 7.7) and 1979 (M_w 8.2) [*Kanamori and McNally*, 1982]. Indeed, in a more global analysis of the circum-Pacific large subduction earthquakes, *Thatcher* [1990] found that this type of behavior might correspond to a systematic pattern with the largest earthquakes being preceded by one or few smaller events (e.g., M_w 7.5–8.0 events preceding a M_w 8.7). In most places, historical catalogs are limited to one or two cycles, or do not have consistent records, and therefore do not allow one to test this hypothesis.

[55] With the exception of the 1960 and 1996 tsunami earthquakes, none of the 6 majors earthquakes of the 1940–2007 sequence seems to have extended closer than 50 km to

the trench. This paucity of shallow earthquakes could be interpreted as evidence for a low degree of plate coupling near the trench. At the latitude of Lima, offshore geodetic data suggests that currently there is in fact little ongoing fault slip on the shallowest part of the plate interface [*Gagnon et al.*, 2005]. This apparent lack of creep is due to interseismic (long-term) coupling, or the effects of a stress shadow associated with a deeper coupled zone [*Bürgmann et al.*, 2005; *Hsu et al.*, 2006; *Hetland et al.*, 2008]. The stress shadow effect implies that the shallow part of the megathurst would experience large amounts of postseismic creep. However, the postseismic GPS campaign made right after the 2007 Pisco earthquake (Perfettini et al., submitted manuscript, 2009) suggest that the upper part of the megathrust fault zone did not experience any afterslip. Alternatively, if this zone is in fact locked and extends over the whole margin of central Peru, the upper part of the megathrust would still be accumulating stresses since the previous large event, supposedly the M 8.6 earthquake of 1746 [*Dorbath et al.*, 1990]. As large events occur on the deepest part of the seismogenic zone (for instance, most of the events of the 1940–2007 sequence) and much less frequently on the shallowest part, it can be speculated that the way the shallow part of the megathrust accumulates stresses is what limits the generation of very large events (M > 8.5). This argument is in line with the observation that the energy released by the 6 event sequence of 1940–2007 does not account for the slip potential accumulated since 1746, even if we assume that only half of the convergence is absorbed by the locked interface [*Norabuena et al.*, 1998]. *Spence et al.* [1999] reached the same conclusion in their study of the segment south of the Nazca ridge which experienced the M_w 8.1 1942 and M_w 7.7, 1996 earthquakes.

6.6. Nazca Ridge as a Barrier to Throughgoing Coseismic Slip

[56] It has been long speculated that short wavelength bathymetric highs have an impact on the coupling of the subduction interface as they descend into the mantle [*Kelleher and McCann*, 1976] with several examples of seamounts or ridges, which are believed to act as barriers to the lateral propagation of rupture [e.g., *Kodaira et al.*, 2000; *Collot et al.*, 2004]. Recent earthquakes (Figure 1) suggest that the Nazca Ridge could be such a permanent barrier.

[57] However, historical reports indicate that two large ruptures might have straddled the ridge, in 1687 and 1868. The details of slip for both events are highly ambiguous. Detailed macroseismic data for the 13 August 1868 Arica earthquake suggest that coseismic rupture stopped south of the ridge, while the destruction of the town of Pisco by the ensuing tsunami, as reported by *Solovev and Go* [1984], suggests the opposite conclusion [*Okal et al.*, 2006]. However, given the confounding effects of local bathymetry can have on tsunami amplification, we tend to favor the scenario wherein slip does not extend across the ridge. The 20 October 1687 earthquake, which strongly affected Lima, is even more unclear, as a second large earthquake might have occurred in southern Peru the same or the following day, therefore creating confusion in the records [*Dorbath et al.*, 1990]. Yet, local historical reports of damage support the idea that the northern area of rupture was bounded to the south by the Nazca ridge [*Dorbath et al.*, 1990], and therefore was roughly equivalent in extent to the 1974 and 2007 ruptures. Besides the chronological confusion with the southern Peru event, which may simply be a date problem, accounts indicate that the 1687 earthquake indeed ruptured in two distinct episodes, the first one destroying Pisco and the second, 2 hours later, destroying Lima [*Dorbath et al.*, 1990]. Assuming that asperities are stable features, as suggested by the gravity-topography analysis of *Song and Simons* [2003] and *Wells et al.* [2003], this would suggest that the 1687 rupture(s) may be equivalent to the 1974 and 2007 events.

[58] From this review of historical events, it seems that none of the identified large historical earthquakes has unequivocally ruptured across the Nazca Ridge. Our slip distribution of the 2007 event, and the models of the 1942 and 1996 ruptures which occurred on the other side of the ridge [*Sennson and Beck*, 1996; *Spence et al.*, 1999; *Swenson and Beck*, 1999; *Salichon et al.*, 2003; *Pritchard et al.*, 2007], indicate that the segment of the Nazca ridge that remains unbroken is about 80 km. This area has experienced several aftershocks, at least following the 2007 rupture, and possibly substantial afterslip according to preliminary processing of campaign GPS data (Perfettini et al., submitted manuscript, 2009). These observations suggest that the character of the Nazca barrier is related to the region-dominant mode of slip in the region being aseismic. However, the recent experience of the Solomons earthquake of 1 April 2007 (M_w 8.1), which ruptured across a subducting Simbo Ridge, may preclude the conclusion that the same type of event will never straddle the Nazca Ridge [*Taylor et al.*, 2008].

6.7. Implications for Tsunami Warning

[59] Without the fortuitous kink of the coastline and the appropriate regularization parameters, it appeared unlikely that the on land geodetic data, would have been able to resolve the distant offshore contour of this rupture, which critically determines its tsunamigenic potential. On the contrary, the modeling of the tsunami open ocean records turned out to be of great sensitivity, and bear out their decisive role in the identification of robust slip distributions, especially in the distant offshore setting of outer rise [e.g., *Fujii and Satake*, 2008], and tsunami earthquakes [e.g., *Fujii and Satake*, 2006]. The NOAA tsunami forecasting system provided accurate estimates of the far-field tsunami amplitudes, but was affected by a 12 min timing error [*Wei et al.*, 2008]. We identified this error as being due to a mislocation of the source, caused by the use of only one tsunameter located in a nonoptimal azimuth [*Hébert et al.*, 2009]. With the densification of the tsunameter network in the Pacific and Indian oceans, most future tsunamis should be recorded in more than one azimuth and in a time delay allowing their direct incorporation in the analysis of the forecast system. However, in some specific locations where the tsunami travel time is relatively short (about 1 or 2 hours), tsunameters density has to be very high to provide systematic and accurate arrival time estimates. Thus, for this type of configuration tsunameter networks might not be the optimal technology. Realtime GPS has been proposed as a viable alternative [*Song*, 2007; *Hoechner et al.*, 2008; *Blewitt et al.*, 2009], but could also be considered to reinforce the reliability of the forecast system (the reliability

and data return ratio of the DART II stations is of 80% or more, http://www.ndbc.noaa.gov/dart/dart2_pc_1.shtml), as well as to improve its accuracy. Another benefit of the realtime GPS data over the tsunameter network is it capacity to also work for near-field tsunami warning systems, in the case of earthquake-induced tsunamis.

7. Conclusion

[60] The joint inversion of teleseismic and high-quality InSAR data enabled us to provide source model of the 2007, Pisco earthquake which adds to the very limited group of well constrained large subduction earthquakes. Our solution is also one of the first to be tested against a combination of field observations, a large local aftershock catalog, as well as open ocean tsunami data. We identified a source composed of two patches with large slip, one located near the epicenter, and a second larger one about 60 km to the South, just offshore the Paracas peninsula (Figure 8). The fact that none of the teleseismic models published online in the aftermath of the earthquake was able to correctly determine the location of the second asperity (two of those models are tested against geodetic data given by *Motagh et al.* [2008]), in conjunction with our three steps analysis (InSAR, teleseismic, joint) gives a good sense of the limited constraints on finite source models provided by teleseismic data when considered alone. In particular, one major characteristic of the 2007 Pisco event which was not resolved by the teleseismic only solutions, is the unusually small extent of the source (60 km) for an event of this magnitude (M_w 8.0). The rather standard duration of the source (60 s) implies that either the earthquake was made of two distinct subevents, or that the rupture had a very slow average rupture velocity. We are not able to discriminate the two possibilities but the hypothesis of two distinct subevents seems more plausible to us. In any case the Pisco earthquake is not a tsunami earthquakes since the geodetic data do not show evidence for any significant aseismic slip.

[61] The ability to obtain a robust slip model of the Pisco earthquake allowed us to explore two major hypotheses on the behavior of subduction zones. The first one, is the suspected tendency of aftershocks to surround the areas of high coseismic slip (Figure 11) in order to homogenize the state of stress on the megathrust. The Pisco earthquake adds to the very limited list of events where this relationship is unequivocally apparent, and seems to be supported by the preliminary analysis of campaign GPS time series which infers afterslip as the mechanism driving the aftershock generation (Perfettini et al., submitted manuscript, 2009). One consequence of the high level of correlation evidenced is the possibility to use aftershock patterns to assess the reliability of the earthquake coseismic models. The second hypothesis confirmed by our study is the relationship between the downdip extent of the large earthquakes and the coastline. In the case of the Pisco earthquake, this link was made evident by the offset of the coastline, also apparent in the coseismic surface deformation computed from our source model (Figure 12). In addition, the anticorrelation of the coseismic surface deformation and the topography suggests that processes of the interseismic phase could directly contribute to the long-term evolution of the bathymetry and topography. The recent multiplication of studies combining geodetic, seismological, tsunami data, etc, is a clear indication that future large earthquake studies will have the opportunity to infer robust rupture models. We expect those models to provide additional evidences of the interconnections between the different phases of the seismic cycles, and to complement results that can be obtained from paleoearthquake and paleotsunami studies [e.g., *Kelsey et al.*, 2006].

[62] Finally, we observed that the Pisco earthquake completed a sequence of large earthquakes initiated in 1940 (Figure 1), which successively ruptured different parts of the central Peru margin up to its now complete coverage. While the North Peru subduction seems to behave quite independently and did not experience any large earthquakes for at least four centuries, the South Peru margin seems to follow a temporal evolution similar to the one of central Peru. One could therefore suspect that the segments north and south of the M 8.4 2001 Arequipa earthquake (Figure 1) would finish to mosaic the South Peru margin.

[63] An important outstanding question is the significance of the change from extremely large events (M 8.5+ in 1687, 1746), to relatively smaller events ($M_w \sim 8.0$) in the 1940–2007 period: is it part of a long-term trend, or simply the repeating characteristic of the seismic cycle in this region? Our limited view of the past earthquakes does not allow us to properly address this question. However, we note that both a global analysis of large earthquakes over the Pacific Ring of Fire [*Thatcher*, 1990], and more regional studies of tsunami deposits in Japan and Chile [*Nanayama et al.*, 2003; *Cisternas et al.*, 2005], both favor the idea that great earthquakes (M_w 8.5+) alternate with periods of relatively smaller earthquakes ($M_w \sim 8$). Moreover, the fact that the 1940–2007 sequence of earthquakes in central Peru does not account for the slip potential accumulated since 1746, indicate that large to very large earthquakes can still be expected in the near future.

Appendix A

A1. InSAR Data and Models

[64] Because of their similar slip distributions, the predicted interferograms for the InSAR-only (Figure A1), joint (Figure A2) and joint with delay (Figure A3) models produce similar residual patterns for the different tracks. These models also require similar ramp corrections.

A2. Effect of Smoothing on the InSAR-Only Inversions

[65] In Figure A4, we show the influence of smoothing (plotted by its inverse, named the roughness) on the slip distribution for the InSAR-only inversions. The smoothest model is made of one large average amplitude slip patch which tends to divide into two more focused asperities as the roughness increase. We do not see large changes in the solution for roughness values above 100, our prefered value. The main evolution is the tendency of the southern patch to divide and create an isolated patch over the Paracas peninsula, an effect that we suspect is related to density of InSAR measurements on the peninsula, as well as their high amplitude. In other words, it is likely that the patch above the peninsula appearing for high roughness values is indeed an artifact of the data distribution.

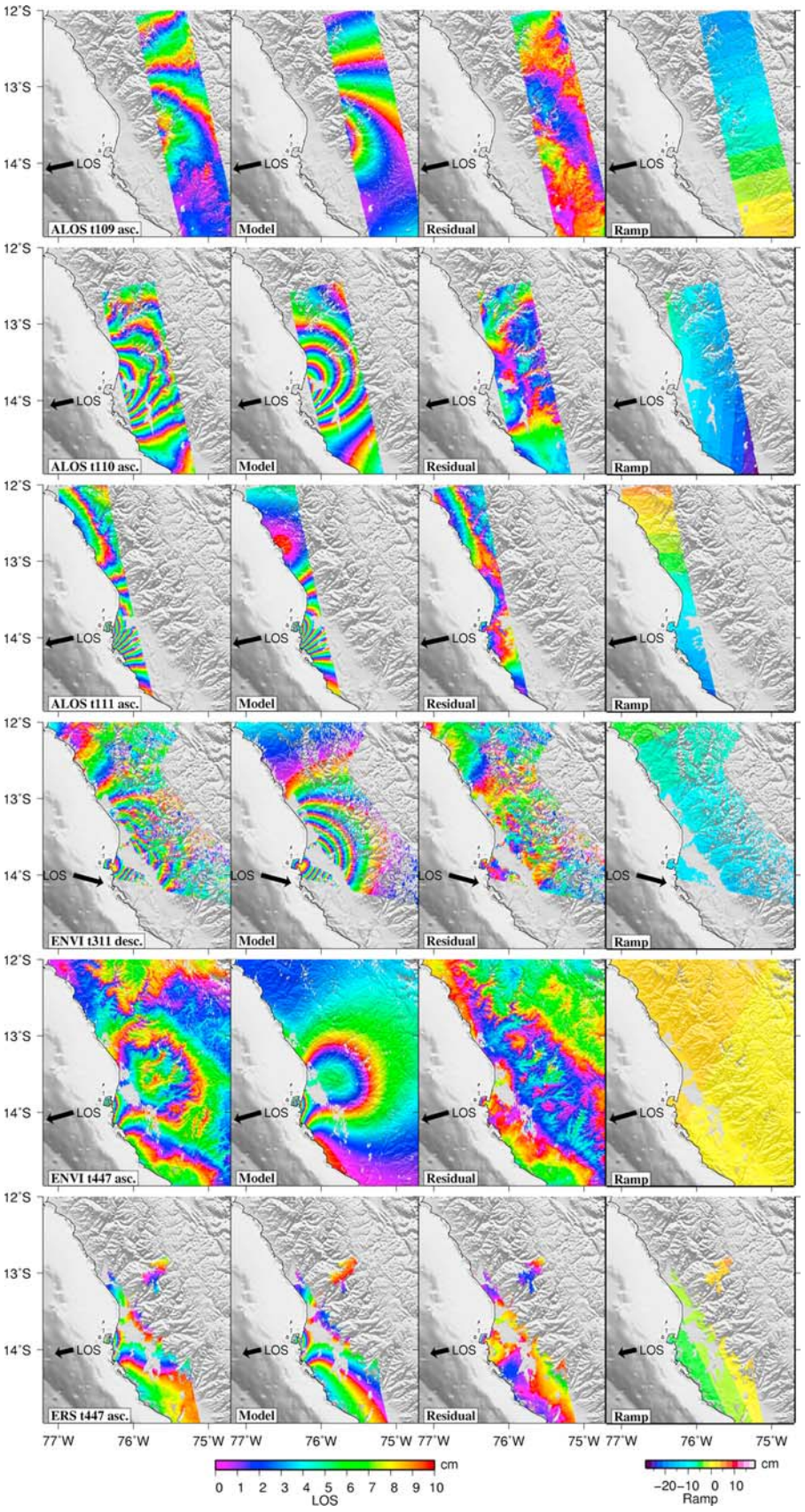

Figure A1. Observed, predicted, residual, and ramp interferograms for the model derived from InSAR data only. The observed data is shown with the ramp removed. All the images are shown with a 10 cm color cycle, except the ramp correction which has it own unwrapped color scale. The black arrow indicates the surface projection of the ground-to-satellite observing direction.

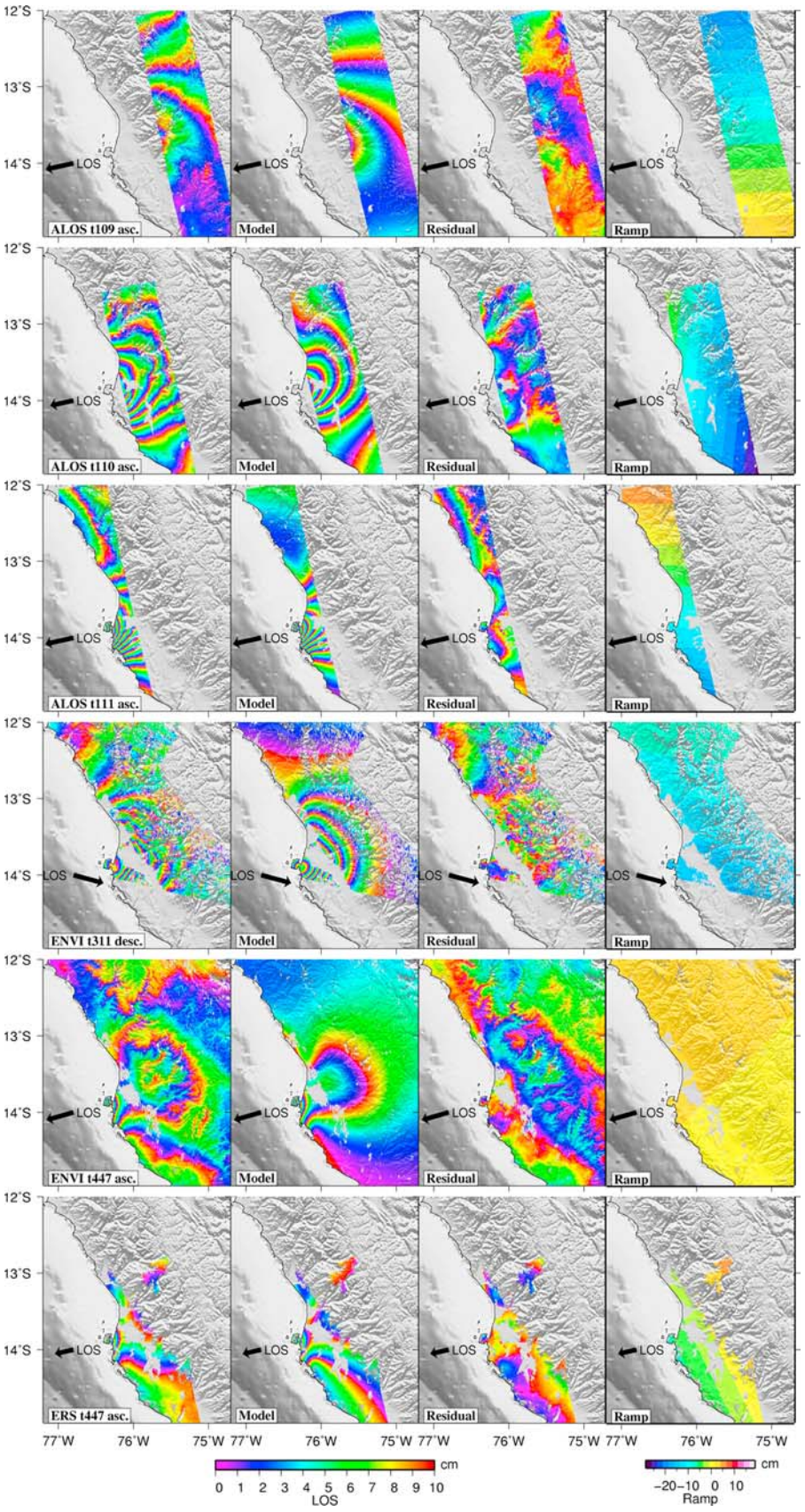

Figure A2. Observed, predicted, residual, and ramp interferograms for the model derived from joint InSAR and teleseismic data. The observed data is shown with the ramp removed. All the images are shown with a 10 cm color cycle, except the ramp correction which has it own unwrapped color scale. The black arrow indicates the surface projection of the ground-to-satellite observing direction.

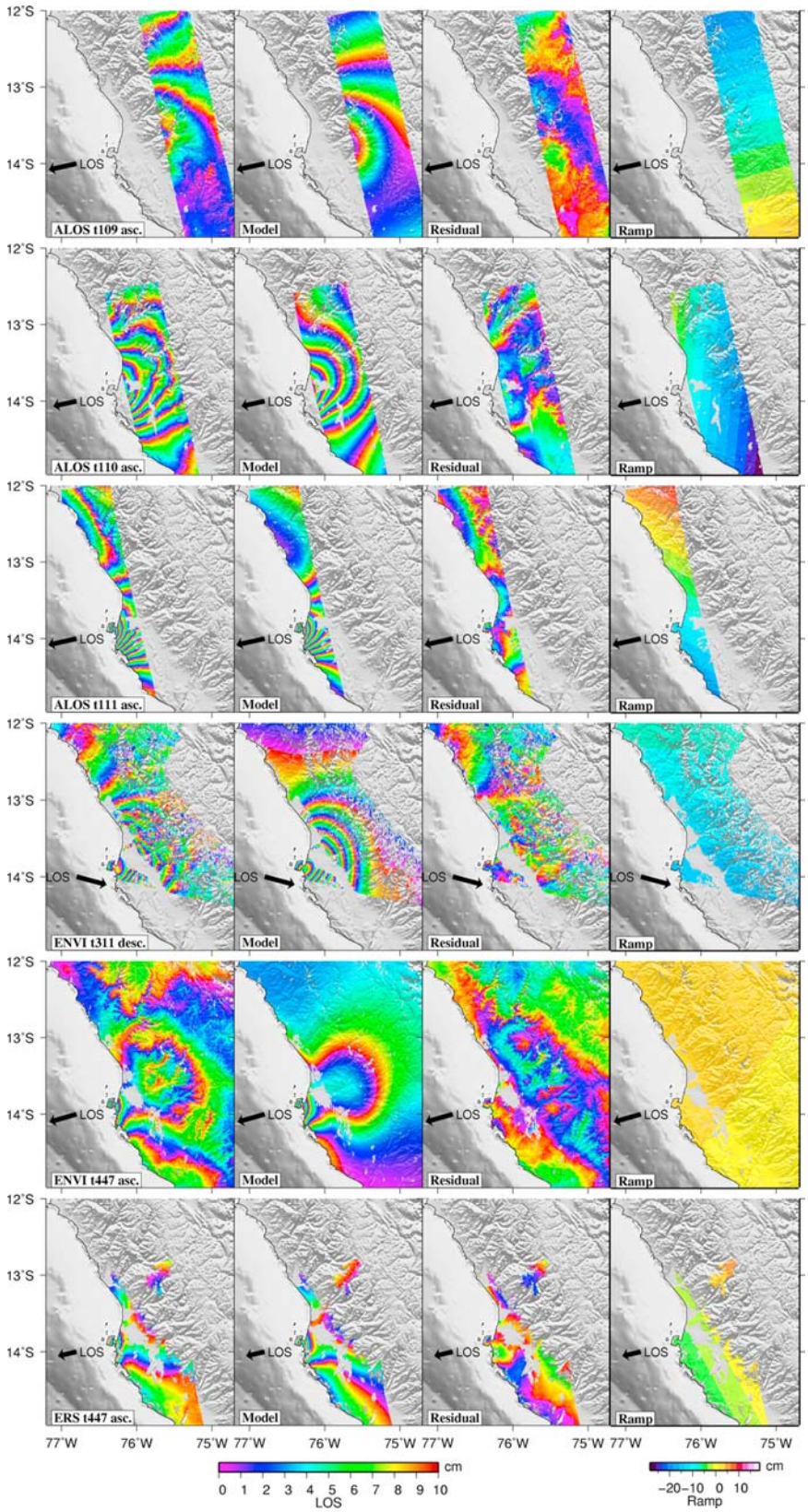

Figure A3. Observed, predicted, residual, and ramp interferograms for a fast rupture model using teleseismic and InSAR data. To compensate the imposed fast rupture velocity (>2.4 km/s), we apply a 38 s time delay between the two deeper fault segments, that is between the two main slip patches. The observed data is shown with the ramp removed. All the images are shown with a 5 cm color cycle, except the ramp correction which has it own unwrapped color scale. The black arrow indicates the surface projection of the ground-to-satellite observing direction.

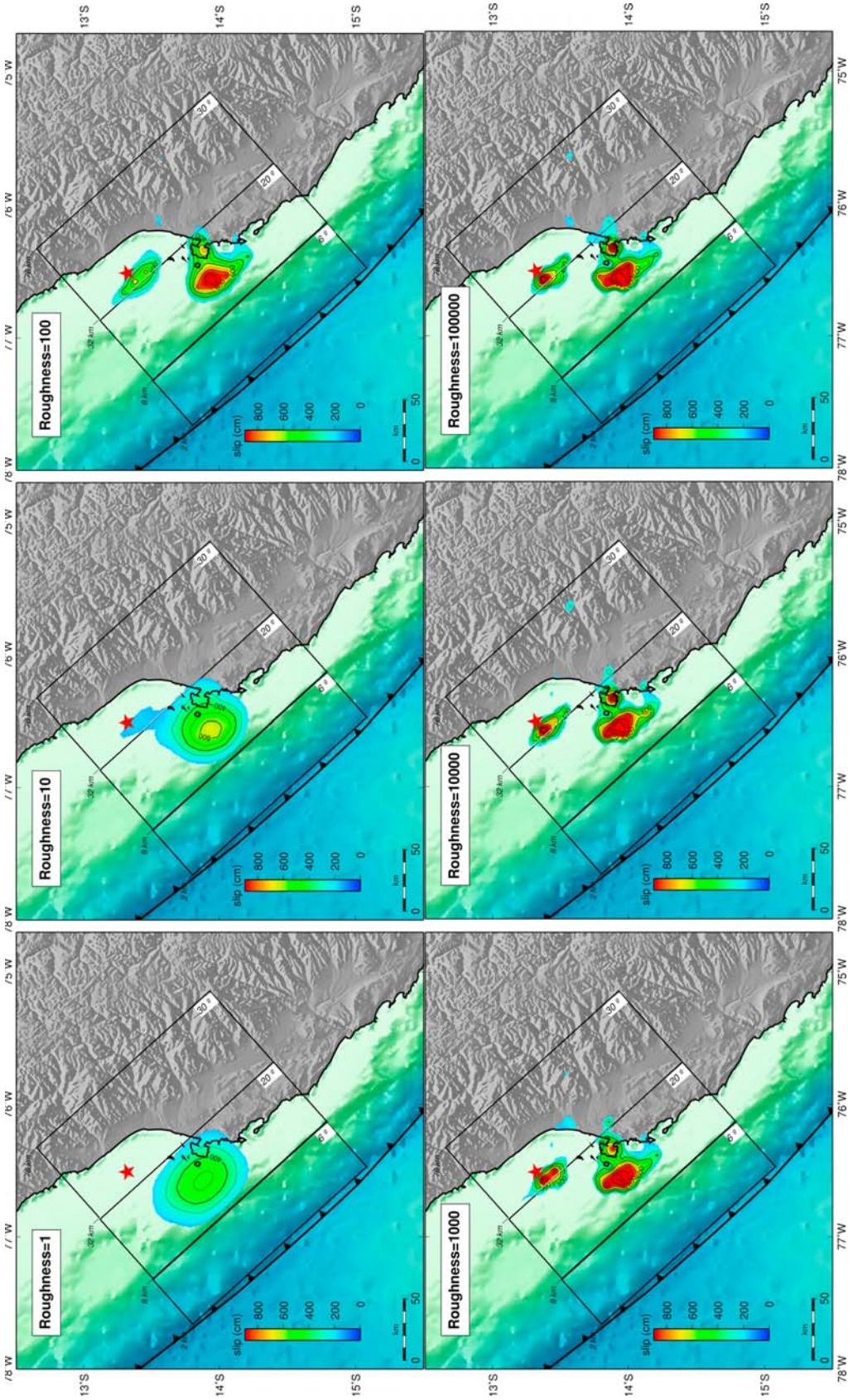

Figure A4. Slip distributions of the Pisco earthquake obtained for different values of the roughness (inverse of the smoothness). According to Figure 5, a roughness coefficient of 100 allows the inversion to converge toward a simple solution and models while maintaining a good fit of the data. This value was used for the analysis presented in the main text.

[66] **Acknowledgments.** We thank two anonymous reviewers for their constructive comments that helped to clarify several points. ERS and Envisat data were provided by ESA under Category 1-3194 (Matthew E. Pritchard) and AOE-668 (E. J. Fielding). ALOS data were provided by the Alaska Satellite Facility and JAXA. Funding for this research was provided by the Gordon and Betty Moore Foundation through the Tectonics Observatory. Part of this research was performed at the Jet Propulsion Laboratory, California Institute of Technology, under contract with the National Aeronautics and Space Administration. Figures have been made using the Generic Mapping Tools (GMT) of *Wessel and Smith* [1998]. This is Caltech Tectonics Observatory contribution 111.

References

Audin, L., and D. Farber (2008), El terremoto de Pisco (Peru) del 15 de Agosto de 2007 (M_w 7.9), in *Direccion de Sismologia*, pp. 439–478, Inst. Geofís. del Perú, Lima.

Audin, L., H. Perfettini, J. Avouac, D. Farber, D. De la Cruz, and M. Chlieh (2007), The 2007 Pisco earthquake (M_w 8.0), central Peru: Preliminary field investigations and seismotectonic context, *Eos Trans. AGU, Fall Meet. Suppl.*, *88*(52), Abstract T33E-02.

Audin, L., P. Lacanb, H. Tavera, and F. Bondoux (2008), Upper plate deformation and seismic barrier in front of Nazca subduction zone: The Chololo Fault System and active tectonics along the coastal cordillera, southern Peru, *Tectonophysics*, *459*(1–4), 174–185, doi:10.1016/j.tecto.2007.11.070.

Bassin, C., G. Laske, and G. Masters (2000), The current limits of resolution for surface wave tomography in North America, *Eos Trans. AGU*, *81*(48), Fall. Meet. Suppl., Abstract S12A-03.

Båth, M. (1965), Lateral inhomogeneities of the upper mantle, *Tectonophysics*, *2*(6), 483–514, doi:10.1016/0040-1951(65)90003-X.

Beck, S. L., and S. P. Nishenko (1990), Variations in the mode of great earthquake rupture along the central Peru subduction zone, *Geophys. Res. Lett.*, *17*, 1969–1972.

Biggs, J., D. P. Robinson, and T. H. Dixon (2009), The 2007 Pisco, Peru, earthquake (M8.0): Seismology and geodesy, *Geophys. J. Int.*, *176*(3), 657–669, doi:10.1111/j.1365-246X.2008.03990.x.

Blewitt, G., W. C. Hammond, C. Kreemer, H. Plag, S. Stein, and E. Okal (2009), GPS for real-time earthquake source determination and tsunami warning systems, *J. Geod.*, *83*(3), 335–343, doi:10.1007/s00190-008-0262-5.

Briggs, R. W., et al. (2008), Persistent elastic behavior above a megathrust rupture patch: Nias island, west Sumatra, *J. Geophys. Res.*, *113*, B12406, doi:10.1029/2008JB005684.

Bürgmann, R., M. G. Kogan, G. M. Steblov, G. Hilley, V. E. Levin, and E. Apel (2005), Interseismic coupling and asperity distribution along the Kamchatka subduction zone, *J. Geophys. Res.*, *110*, B07405, doi:10.1029/2005JB003648.

Cahill, T., and B. L. Isacks (1992), Seismicity and shape of the subducted Nazca plate, *J. Geophys. Res.*, *97*(B12), 17,503–17,529.

Cisternas, M., et al. (2005), Predecessors of the giant 1960 Chile earthquake, *Nature*, *437*(7057), 404–407, doi:10.1038/nature03943.

Clift, P. D., I. Pecher, N. Kukowski, and A. Hampel (2003), Tectonic erosion of the Peruvian forearc, Lima basin, by subduction and Nazca ridge collision, *Tectonics*, *22*(3), 1023, doi:10.1029/2002TC001386.

Collot, J., B. Marcaillou, F. Sage, F. Michaud, W. Agudelo, P. Charvis, D. Graindorge, M. Gutscher, and G. Spence (2004), Are rupture zone limits of great subduction earthquakes controlled by upper plate structures? Evidence from multichannel seismic reflection data acquired across the northern Ecuador–southwest Colombia margin, *J. Geophys. Res.*, *109*, B11103, doi:10.1029/2004JB003060.

Console, R., A. M. Lombardi, M. Murru, and D. Rhoades (2003), Båth's law and the self-similarity of earthquakes, *J. Geophys. Res.*, *108*(B2), 2128, doi:10.1029/2001JB001651.

Das, S., and C. Henry (2003), Spatial relation between main earthquake slip and its aftershock distribution, *Rev. Geophys.*, *41*(3), 1013, doi:10.1029/2002RG000119.

Delouis, B., M. Pardo, D. Legrand, and T. Monfret (2009), The M_w 7.7 Tocopilla earthquake of 14 November 2007 at the southern edge of the northern Chile seismic gap: Rupture in the deep part of the coupled plate interface, *Bull. Seismol. Soc. Am.*, *99*(1), 87–94, doi:10.1785/0120080192.

Dewey, J. W., and W. Spence (1979), Seismic gaps and source zones of recent large earthquakes in coastal Peru, *Pure Appl. Geophys.*, *117*(6), 1148–1171, doi:10.1007/BF00876212.

Dorbath, L., A. Cisternas, and C. Dorbath (1990), Assessment of the size of large and great historical earthquakes in Peru, *Bull. Seismol. Soc. Am.*, *80*(3), 551–576.

Farr, T., et al. (2007), The shuttle radar topography mission, *Rev. Geophys.*, *45*, RG2004, doi:10.1029/2005RG000183.

Fritz, H. M., N. Kalligeris, J. C. Borrero, P. Broncano, and E. Ortega (2008), The 15 August 2007 Peru tsunami runup observations and modeling, *Geophys. Res. Lett.*, *35*, L10604, doi:10.1029/2008GL033494.

Fujii, Y., and K. Satake (2006), Source of the July 2006 west Java tsunami estimated from tide gauge records, *Geophys. Res. Lett.*, *33*, L24317, doi:10.1029/2006GL028049.

Fujii, Y., and K. Satake (2008), Tsunami sources of the November 2006 and January 2007 great Kuril earthquakes, *Bull. Seismol. Soc. Am.*, *98*(3), 1559–1571, doi:10.1785/0120070221.

Fukao, Y. (1979), Tsunami earthquakes and subduction processes near deep-sea trenches, *J. Geophys. Res.*, *84*, 2303–2314.

Fuller, C. W., S. D. Willett, and M. T. Brandon (2006), Formation of forearc basins and their influence on subduction zone earthquakes, *Geology*, *34*(2), 65–68, doi:10.1130/G21828.1.

Gagnon, K., C. D. Chadwell, and E. Norabuena (2005), Measuring the onset of locking in the Peru-Chile trench with GPS and acoustic measurements, *Nature*, *434*(7030), 205–208, doi:10.1038/nature03412.

Grevemeyer, I., and V. M. Tiwari (2006), Overriding plate controls spatial distribution of megathrust earthquakes in the Sunda–Andaman subduction zone, *Earth Planet. Sci. Lett.*, *251*(3–4), 199–208.

Hartzell, S., and C. Langer (1993), Importance of model parameterization in finite fault inversions: Application to the 1974 M_w 8.0 Peru earthquake, *J. Geophys. Res.*, *98*(B12), 22,123–22,134.

Hébert, H., P. Heinrich, F. Schindelé, and A. Piatanesi (2001), Far-field simulation of tsunami propagation in the Pacific Ocean: Impact on the Marquesas islands (French Polynesia), *J. Geophys. Res.*, *106*, 9161–9178.

Hébert, H., D. Reymond, Y. Krien, J. Vergoz, F. Schindelé, J. Roger, and A. Loevenbruck (2009), The 15 August 2007 Peru earthquake and tsunami: Influence of the Source Characteristics on the Tsunami Heights, *Pure Appl. Geophys.*, *166*(1–2), 211–232.

Heinrich, P., F. Schindele, S. Guibourg, and P. F. Ihmlé (1998), Modeling of the February 1996 Peruvian tsunami, *Geophys. Res. Lett.*, *25*(14), 2687–2690.

Hetland, E., M. Simons, E. M. Dunham, and R. V. Kanda (2008), Interseismic deformation and the mechanical behavior of megathrusts: Transient postseismic creep, stress shadows, and megathrust rheology, in *Eos Trans. AGU, Fall Meet. Suppl.*, *89*(53), Abstract T12A-04.

Hoechner, A., A. Y. Babeyko, and S. V. Sobolev (2008), Enhanced GPS inversion technique applied to the 2004 Sumatra earthquake and tsunami, *Geophys. Res. Lett.*, *35*, L08310, doi:10.1029/2007GL033133.

Hsu, Y., M. Simons, J. Avouac, J. Galetzka, K. Sieh, M. Chlieh, D. Natawidjaja, L. Prawirodirdjo, and Y. Bock (2006), Frictional afterslip following the 2005 Nias-Simeulue earthquake, Sumatra, *Science*, *312*(5782), 1921–1926, doi:10.1126/science.1126960.

Ji, C., D. J. Wald, and D. V. Helmberger (2002), Source description of the 1999 Hector mine, California, earthquake, part I: Wavelet domain inversion theory and resolution analysis, *Bull. Seismol. Soc. Am.*, *92*(4), 1192–1207, doi:10.1785/0120000916.

Kanamori, H. (1972), Mechanism of tsunami earthquakes, *Phys. Earth Planet. In.*, *6*(5), 346–359, doi:10.1016/0031-9201(72)90058-1.

Kanamori, H., and J. W. Given (1981), Use of long-period surface waves for rapid determination of earthquake source parameters, *Phys. Earth Planet. Inter.*, *27*(1), 8–31.

Kanamori, H., and K. C. McNally (1982), Variable rupture mode of the subduction zone along the Ecuador-Colombia coast, *Bull. Seismol. Soc. Am.*, *72*(4), 1241–1253.

Kelleher, J., and W. McCann (1976), Buoyant zones, great earthquakes, and unstable boundaries of subduction, *J. Geophys. Res.*, *81*(B26), 4885–4896.

Kelsey, H., K. Satake, Y. Sawai, B. Sherrod, K. Shimokawa, and M. Shishikura (2006), Recurrence of postseismic coastal uplift, Kuril subduction zone, Japan, *Geophys. Res. Lett.*, *33*, L13315, doi:10.1029/2006GL026052.

Kim, A., and D. S. Dreger (2008), Rupture process of the 2004 Parkfield earthquake from near-fault seismic waveform and geodetic records, *J. Geophys. Res.*, *113*, B07308, doi:10.1029/2007JB005115.

King, G. C. P., R. S. Stein, and J. B. Rundle (1998), The growth of geological structures by repeated earthquakes: 1. Conceptual framework, *J. Geophys. Res.*, *93*(B11), 13,307–13,318.

Kodaira, S., N. Takahashi, A. Nakanishi, S. Miura, and Y. Kaneda (2000), Subducted seamount imaged in the rupture zone of the 1946 Nankaido earthquake, *Science*, *289*(5476), 104–106, doi:10.1126/science.289.5476.104.

Koketsu, K., K. Hikima, S. Miyazaki, and S. Ide (2004), Joint inversion of strong motion and geodetic data for the source process of the 2003 Tokachi-Oki, Hokkaido, earthquake, *Earth Planets Space*, *56*, 329–334.

Konca, A. O., V. Hjorleifsdottir, T. A. Song, J. Avouac, D. V. Helmberger, C. Ji, K. Sieh, R. Briggs, and A. Meltzner (2007), Rupture kinematics of the 2005 M_w 8.6 Nias-Simeulue earthquake from the joint inversion of seismic and geodetic data, *Bull. Seismol. Soc. Am.*, *97*(1A), S307–S322, doi:10.1785/0120050632.

Konca, A. O., et al. (2008), Partial rupture of a locked patch of the sumatra megathrust during the 2007 earthquake sequence, *Nature*, *456*(7222), 631–635, doi:10.1038/nature07572.

Krabbenhoft, A., J. Bialas, H. Kopp, N. Kukowski, and C. Hubscher (2004), Crustal structure of the Peruvian continental margin from wide-angle seismic studies, *Geophys. J. Int.*, *159*(2), 749–764, doi:10.1111/j.1365-246X.2004.02425.x.

Langer, C. J., and W. Spence (1995), The 1974 Peru earthquake series, *Bull. Seismol. Soc. Am.*, *85*(3), 665–687.

Lohman, R. B., and M. Simons (2005), Some thoughts on the use of InSAR data to constrain models of surface deformation: Noise structure and data downsampling, *Geochem. Geophys. Geosyst.*, *6*, Q01007, doi:10.1029/2004GC000841.

Miyagi, Y., Y. Nishimura, H. Takahashi, and M. Shimada (2007), Crustal deformation caused by earthquake detected by InSAR technique using ALOS/PALSAR data, in *Eos Trans. AGU*, *88*(52), Fall Meet. Suppl., Abstract G51C-0619.

Miyazaki, S., P. Segall, J. Fukuda, and T. Kato (2004), Space time distribution of afterslip following the 2003 Tokachi-Oki earthquake: Implications for variations in fault zone frictional properties, *Geophys. Res. Lett.*, *31*, L06623, doi:10.1029/2003GL019410.

Motagh, M., R. Wang, T. R. Walter, R. Brgmann, E. Fielding, J. Anderssohn, and J. Zschau (2008), Coseismic slip model of the 2007 August Pisco earthquake (Peru) as constrained by wide swath radar observations, *Geophys. J. Int.*, *174*(3), 842–848, doi:10.1111/j.1365-246X.2008.03852.x.

Nanayama, F., K. Satake, R. Furukawa, K. Shimokawa, B. Atwater, K. Shigeno, and S. Yamaki (2003), Unusually large earthquakes inferred from tsunami deposits along the Kuril trench, *Nature*, *424*(6949), 660–663, doi:10.1038/nature01864.

Nelson, A. R., Y. Sawai, A. E. Jennings, L. Bradley, L. Gerson, B. L. Sherrod, J. Sabean, and B. P. Horton (2008), Great-earthquake paleogeodesy and tsunamis of the past 2000 years at Alsea bay, central Oregon coast, USA, *Quat. Sci. Rev.*, *27*(7–8), 747–768, doi:10.1016/j.quascirev.2008.01.001.

Norabuena, E., L. Leffler-Griffin, A. Mao, T. Dixon, S. Stein, I. S. Sacks, L. Ocola, and M. Ellis (1998), Space geodetic observations of Nazca-South America convergence across the central Andes, *Science*, *279*(5349), 358–362, doi:10.1126/science.279.5349.358.

Okal, E., and A. V. Newman (2001), Tsunami earthquakes: The quest for a regional signal, *Phys. Earth Planet. Inter.*, *124*, 45–70, doi:10.1016/S0031-9201(01)00187-X.

Okal, E. A. (1988), Seismic parameters controlling far-field tsunami amplitudes: A review, *Nat. Hazards*, *1*(1), 67–96, doi:10.1007/BF00168222.

Okal, E. A. (1992), Use of the mantle magnitude Mm for the reassessment of the moment of historical earthquakes, *Pure Appl. Geophys.*, *139*(1), 17–57, doi:10.1007/BF00876825.

Okal, E. A., J. C. Borrero, and C. E. Synolakis (2006), Evaluation of tsunami risk from regional earthquakes at Pisco, Peru, *Bull. Seismol. Soc. Am.*, *96*(5), 1634–1648, doi:10.1785/0120050158.

Perfettini, H., and J. Ampuero (2008), Dynamics of a velocity strengthening fault region: Implications for slow earthquakes and postseismic slip, *J. Geophys. Res.*, *113*, B09411, doi:10.1029/2007JB005398.

Perfettini, H., and J. P. Avouac (2004), Stress transfer and strain rate variations during the seismic cycle, *J. Geophys. Res.*, *109*, B06402, doi:10.1029/2003JB002917.

Perfettini, H., J. P. Avouac, and J. C. Ruegg (2005), Geodetic displacements and aftershocks following the 2001 M_w = 8.4 Peru earthquake: Implications for the mechanics of the earthquake cycle along subduction zones, *J. Geophys. Res.*, *110*, B09404, doi:10.1029/2004JB003522.

Pritchard, M. E., and E. J. Fielding (2008), A study of the 2006 and 2007 earthquake sequence of Pisco, Peru, with InSAR and teleseismic data, *Geophys. Res. Lett.*, *35*, L09308, doi:10.1029/2008GL033374.

Pritchard, M. E., M. Simons, P. A. Rosen, S. Hensley, and F. H. Webb (2002), Co-seismic slip from the 1995 July 30 M_w 8.1 Antofagasta, Chile, earthquake as constrained by InSAR and GPS observations, *Geophys. J. Int.*, *150*(2), 362–376, doi:10.1046/j.1365-246X.2002.01661.x.

Pritchard, M. E., E. O. Norabuena, C. Ji, R. Boroschek, D. Comte, M. Simons, T. H. Dixon, and P. A. Rosen (2007), Geodetic, teleseismic, and strong motion constraints on slip from recent southern Peru subduction zone earthquakes, *J. Geophys. Res.*, *112*, B03307, doi:10.1029/2006JB004294.

Rosen, P. A., S. Henley, G. Peltzer, and M. Simons (2004), Updated repeat orbit interferometry package released, *Eos Trans. AGU*, *85*(5), doi:10.1029/2004EO050004.

Ruff, L. J., and B. Tichelaar (1996), What controls the seismogenic plate interface in subduction zones?, in *Subduction: Top to Bottom*, *Geophys. Monogr. Ser.*, vol. 96, edited by G. E. Bebout et al., pp. 105–111, AGU, Washington, DC.

Salichon, J., B. Delouis, P. Lundgren, D. Giardini, M. Costantini, and P. Rosen (2003), Joint inversion of broadband teleseismic and interferometric synthetic aperture radar (InSAR) data for the slip history of the M_w = 7.7, Nazca ridge (Peru) earthquake of 12 November 1996, *J. Geophys. Res.*, *108*(B2), 2085, doi:10.1029/2001JB000913.

Savage, J. (1983), A dislocation model of strain accumulation and release at a subduction zone, *J. Geophys. Res.*, *88*(B6), 4984–4996.

Scott, D. W. (1992), *Multivariate Density Estimation*, 317 pp., Wiley, New York.

Sella, G. F., T. H. Dixon, and A. Mao (2002), REVEL: A model for recent plate velocities from space geodesy, *J. Geophys. Res.*, *107*(B4), 2081, doi:10.1029/2000JB000033.

Sennson, J. L., and S. L. Beck (1996), Historical 1942 Ecuador and 1942 Peru subduction earthquakes and earthquake cycles along Colombia-Ecuador and Peru subduction segments, *Pure Appl. Geophys.*, *146*(1), 67–101, doi:10.1007/BF00876670.

Simoes, M., J. Avouac, R. Cattin, and P. Henry (2004), The Sumatra subduction zone: A case for a locked fault zone extending into the mantle, *J. Geophys. Res.*, *109*, B10402, doi:10.1029/2003JB002958.

Singh, S., et al. (2008), Seismic evidence for broken oceanic crust in the 2004 Sumatra earthquake epicentral region, *Nature Geosci.*, *1*(11), 777–781, doi:10.1038/ngeo336.

Sladen, A., et al. (2008), Interplay between large earthquakes and coastal geomorphology: Insight from the 2007 Pisco earthquake (M_w = 8.0), central Peru, *Eos Trans. AGU*, *89*(23), Jt. Assem. Suppl., Abstract S23A-04.

Smith, W. H., and D. T. Sandwell (1997), Global seafloor topography from satellite altimetry and ship depth soundings, *Science*, *277*(5334), 1956–1962, doi:10.1126/science.277.5334.1956.

Solovev, S. L., and C. N. Go (1984), *A Catalog of Tsunamis on the East Coast of the Pacific*, vol. 5078, 285 pp., Dep. of the Secr. of the State of Can., Sidney, B. C., Canada.

Song, T. A., and M. Simons (2003), Large Trench-Parallel gravity variations predict seismogenic behavior in subduction zones, *Science*, *301*(5633), 630–633, doi:10.1126/science.1085557.

Song, Y. (2007), Detecting tsunami genesis and scales directly from coastal GPS stations, *Geophys. Res. Lett.*, *34*, L19602, doi:10.1029/2007GL031681.

Song, Y. T., L. Fu, V. Zlotnicki, C. Ji, V. Hjorleifsdottir, C. Shum, and Y. Yi (2008), The role of horizontal impulses of the faulting continental slope in generating the 26 December 2004 tsunami, *Ocean Modell.*, *20*(4), 362–379, doi:10.1016/j.ocemod.2007.10.007.

Spence, W., C. Mendoza, E. R. Engdahl, G. L. Choy, and E. Norabuena (1999), Seismic subduction of the Nazca ridge as shown by the 1996–97 Peru earthquakes, *Pure Appl. Geophys.*, *154*(3), 753–776, doi:10.1007/s000240050251.

Suwa, Y., S. Miura, A. Hasegawa, T. Sato, and K. Tachibana (2006), Interplate coupling beneath NE Japan inferred from three-dimensional displacement field, *J. Geophys. Res.*, *111*, B04402, doi:10.1029/2004JB003203.

Swenson, J. L., and S. L. Beck (1999), Source characteristics of the 12 November 1996 M_w 7.7 Peru subduction zone earthquake, *Pure Appl. Geophys.*, *154*(3), 731–751, doi:10.1007/s000240050250.

Tanioka, Y., and K. Satake (1996), Tsunami generation by horizontal displacement of ocean bottom, *Geophys. Res. Lett.*, *23*(8), 861–864.

Tassara, A., H. J. Gotze, S. Schmidt, and R. Hackney (2006), Three-dimensional density model of the Nazca plate and the Andean continental margin, *J. Geophys. Res.*, *111*, B09404, doi:10.1029/2005JB003976.

Tavera, H., and I. Bernal (2008), The Pisco (Peru) earthquake of 15 August 2007, *Seismol. Res. Lett.*, *79*(4), 510–515, doi:10.1785/gssrl.79.4.510.

Taylor, F. W., R. W. Briggs, C. Frohlich, A. Brown, M. Hornbach, A. K. Papabatu, A. J. Meltzner, and D. Billy (2008), Rupture across arc segment and plate boundaries in the 1 April 2007 Solomons earthquake, *Nat. Geosci.*, *1*(4), 253–257, doi:10.1038/ngeo159.

Thatcher, W. (1990), Order and diversity in the modes of circum-Pacific earthquake recurrence, *J. Geophys. Res.*, *95*(B3), 2609–2623.

Tichelaar, B. W., and L. J. Ruff (1993), Depth of seismic coupling along subduction zones, *J. Geophys. Res.*, *98*(B2), 2017–2037.

Von Huene, R., and S. Lallemand (1990), Tectonic erosion along the Japan and Peru convergent margins, *Geol. Soc. Am. Bull.*, *102*(6), 704–720, doi:10.1130/0016-7606(1990)102.

Von Huene, R., and D. W. Scholl (1991), Observations at convergent margins concerning sediment subduction, subduction erosion, and the growth of continental crust, *Rev. Geophys.*, *29*(3), 279–316, doi:10.1029/91RG00969.

Wei, Y., E. N. Bernard, L. Tang, R. Weiss, V. V. Titov, C. Moore, M. Spillane, M. Hopkins, and M. Kânoğlu (2008), Real-time experimental forecast of the Peruvian tsunami of August 2007 for US coastlines, *Geophys. Res. Lett.*, *35*, L04609, doi:10.1029/2007GL032250.

Weinstein, S. A., and E. A. Okal (2005), The mantle magnitude mm and the slowness parameter theta: Five years of Real-Time use in the context of tsunami warning, *Bull. Seismol. Soc. Am.*, *95*(3), 779–799, doi:10.1785/0120040112.

Wells, D. L., and K. J. Coppersmith (1994), New empirical relationships among magnitude, rupture length, rupture width, rupture area, and surface displacement, *Bull. Seismol. Soc. Am.*, *84*, 974–1002.

Wells, R. E., R. J. Blakely, Y. Sugiyama, D. W. Scholl, and P. A. Dinterman (2003), Basin-centered asperities in great subduction zone earthquakes: A link between slip, subsidence, and subduction erosion?, *J. Geophys. Res.*, *108*(B10), 2507, doi:10.1029/2002JB002072.

Wessel, P., and W. H. F. Smith (1998), New, improved version of the Generic Mapping Tools released, *Eos Trans. AGU*, *79*(47), 579.

Woessner, J., D. Schorlemmer, S. Wiemer, and P. M. Mai (2006), Spatial correlation of aftershock locations and on-fault main shock properties, *J. Geophys. Res.*, *111*, B08301, doi:10.1029/2005JB003961.

Xie, X., and Z. X. Yao (1989), A generalized reflection-transmission coefficient matrix method to calculate static displacement field of a dislocation source in a stratified half-space, *Chin. J. Geophys.*, *32*, 191–205.

L. Audin, LMTG, Université de Toulouse, UPS, 38 Rue des 36 Ponts, F-31400 Toulouse, France.

J. P. Avouac and A. Sladen, Tectonics Observatory, Division of Geological and Planetary Sciences, California Institute of Technology, 1200 E. California Blvd., MC 100-23, Pasadena, CA 91125-2300, USA. (sladen@gps.caltech.edu)

R. Cavagnoud, Instituto Francés de Estudios Andinos, Av. Arequipa 4500, Miraflores, Lima 18, Peru.

E. J. Fielding, Jet Propulsion Laboratory, California Institute of Technology, 4800 Oak Grove Dr., Pasadena, CA 91109, USA.

A. O. Konca, F. Ortega, and M. Simons, Seismological Laboratory, California Institute of Technology, 1200 E. California Blvd., MS 252-21, Pasadena, CA 91125-2100, USA.

H. Perfettini, Laboratoire de Géophysique Interne et de Tectonophysique, Université Joseph Fourier, IRD, BP 53, F-38041 Grenoble CEDEX 9, France.

H. Tavera, Instituto Geofísico del Perú, Calle Badajoz 169 Urb., Mayorazgo IV Etapa ATE, Lima, Peru.